ADAPTIVE ARTIFICIAL ANTI-DIFFUSION METHODS FOR HYPERBOLIC SYSTEMS OF CONSERVATION LAWS*

SHAOSHUAI CHU†, IGOR KLIAKHANDLER‡, AND ALEXANDER KURGANOV§

Abstract. We introduce new adaptive artificial anti-diffusion (AAAD) methods for one- and two-dimensional hyperbolic systems of conservation laws. The key idea is to reduce the amount of numerical dissipation present in a given numerical method by adding an anti-diffusion (AD) term acting in linearly degenerate fields only. This way, the resolution of contact waves can be improved without risking oscillations, which may be caused if the AD acts in nonlinear fields as well. The AD coefficients are selected adaptively: they are supposed to be proportional to the mesh size near the contact waves to enhance the resolution and to be very small in the smooth parts of the computed solution to ensure a sufficiently high (formal) order of accuracy there. The proposed AAAD methods are realized using either the second-order central-upwind numerical fluxes or their fifth-order extensions implemented within the alternative weighted essentially non-oscillatory (A-WENO) framework. We test the proposed schemes on a series of benchmarks for the one- and two-dimensional Euler equations of gas dynamics and the obtained results demonstrate the robustness and high resolution of the new AAAD methods.

Key words. Adaptive artificial anti-diffusion; central-upwind schemes; A-WENO schemes; Euler equations of gas dynamics.

MSC codes. 65M08, 65M06, 76M12, 76M20, 76L05, 35L65

1. Introduction.

This paper focuses on numerical solutions of hyperbolic systems of conservation laws, which in the one-dimensional (1-D) and two-dimensional (2-D) cases, read as

$$\boldsymbol{U}_t + \boldsymbol{F}(\boldsymbol{U})_x = \boldsymbol{0}, \tag{1.1}$$

and

$$\boldsymbol{U}_t + \boldsymbol{F}(\boldsymbol{U})_x + \boldsymbol{G}(\boldsymbol{U})_y = \boldsymbol{0}, \tag{1.2}$$

where t denotes time, x and y are spatial coordinates, $\boldsymbol{U} \in \mathbb{R}^d$ is the vector of conserved variables, and $\boldsymbol{F}, \boldsymbol{G} : \mathbb{R}^d \to \mathbb{R}^d$ are the flux functions.

It is well-known that even for smooth initial data, solutions of (1.1) and (1.2) may develop complicated wave patterns containing shock waves, rarefaction waves, and contact discontinuities. The presence of such nonsmooth structures makes the design of accurate and robust numerical methods particularly challenging. On the one hand, a good scheme has to suppress nonphysical oscillations near discontinuities in order to remain stable. On the other hand, it must retain sufficient resolution so that physically relevant structures are not over-smeared by excessive numerical dissipation. Achieving this balance between robustness and low numerical dissipation is one of the central difficulties in the development of numerical methods for hyperbolic conservation laws.

A classical approach to enforce stability is to add an artificial viscosity (AV) to the underlying unstable (or, only linearly stable) numerical scheme. Since its introduction in [46], this idea has been successfully used in many works; see, e.g., [3,17,20,21,26,43,51] to name just a few. The main advantage of AV methods lies in their simplicity and robustness, since they provide an effective mechanism for suppressing spurious oscillations and enhancing nonlinear stability. However, designing a successful AV method remains a delicate task. On the one hand, a sufficient amount of AV must be added near discontinuities in order to suppress spurious oscillations and guarantee nonlinear stability. If it is too small, the added AV may be insufficient to stabilize the computation near discontinuities, and nonphysical oscillations may still

*Submitted to the editors DATE???.

Funding: The work of S. Chu was funded by the DFG–SPP 2183: Eigenschaftsgeregelte Umformprozesse with the Project(s) HE5386/19-2,19-3 Entwicklung eines flexiblen isothermen Reckschmiedeprozesses für die eigenschaftsgeregelte Herstellung von Turbinenschaufeln aus Hochtemperaturwerkstoffen (424334423) and by the Deutsche Forschungsgemeinschaft (DFG, German Research Foundation)–SPP 2410 Hyperbolic Balance Laws in Fluid Mechanics: Complexity, Scales, Randomness (CoScaRa) within the Project(s) HE5386/27-1 (Zufällige kompressible Euler Gleichungen: Numerik und ihre Analysis, 525853336). The work of A. Kurganov was supported in part by NSFC grant W2431004.

†Department of Mathematics, RWTH Aachen University, Aachen, 52056, Germany (chu@igpm.rwth-aachen.de).

‡Department of Mathematics, Michigan Technological University, Houghton, MI 49931, USA (igor@mtu.edu).

§Department of Mathematics and Shenzhen International Center for Mathematics, Southern University of Science and Technology, Shenzhen, 518055, China (alexander@sustech.edu.cn).

occur. On the other hand, the added AV should remain sufficiently small in smooth regions so that the high-order accuracy of the underlying scheme is not destroyed. If it is too large, the numerical solution may become excessively diffused, leading to a substantial loss of resolution. Therefore, in order to achieve both robustness and high resolution, the AV must be introduced adaptively, based on a suitable smoothness indicator (SI) capable of detecting "rough" parts of the computed solution and determining the appropriate amount of AV to be added there. This has been done, for instance, in [17, 26], but even these advanced adaptive artificial viscosity (AAV) methods do not achieve the same level of resolution achieved by modern shock-capturing methods.

In high-resolution shock-capturing methods, stability is achieved by incorporating nonlinear limiters into the reconstruction or flux evaluation procedures. This strategy has proved to be highly effective and underlies many robust non-oscillatory methods. However, the robustness gained in this way is often accompanied by increased numerical dissipation. In particular, contact discontinuities and small-scale smooth structures may become noticeably smeared, especially on relatively coarse meshes. Therefore, for numerical methods that already employ nonlinear limiters, it is natural to seek a mechanism that improves resolution without destroying a non-oscillatory property ensured by the limiter.

In this paper, we develop a new class of adaptive artificial anti-diffusion (AAAD) methods for hyperbolic systems of conservation laws. Our starting point is somewhat similar to the AAV philosophy, but rather than locally increasing the amount of numerical diffusion, we adaptively add suitable anti-diffusive (AD) corrections to enhance the resolution of the scheme, which is already stabilized by nonlinear limiters. In this way, the nonlinear limiters continue to control spurious oscillations, while the AD terms compensate excessive numerical diffusion. This is particularly advantageous near contact discontinuities, whose accurate resolution is often degraded by the numerical diffusion inherent in shock-capturing schemes.

A key point in our construction is that the AD correction is applied in linearly degenerate characteristic fields only. This allows us to sharpen contact waves without introducing undesirable oscillations into the genuinely nonlinear fields associated with shocks and rarefactions. Another essential feature of the proposed AAAD method is adaptivity. The AD coefficients are chosen so that the correction is sufficiently strong only in "rough" regions, while remaining very small in smooth parts of the computed solution. As a result, the designed (formal) order of accuracy of the underlying scheme is retained in smooth regions, whereas the resolution of contact discontinuities is significantly enhanced.

To adjust the AAAD coefficients, we need to automatically detect the "rough" parts of the computed solution with the help of an SI. Many different SIs are readily available; see, e.g., [1,5,9–14,18,23,35,37,38, 47,49,50] and references therein. In this paper, we employ the recently proposed modified minmod-based SI introduced in [7], which is a modified version of the minmod-based SI from [49]; see also [19, 42]. We apply this SI to different fields in order to automatically distinguish contact waves from other "rough" parts of the solution. For example, in the case of the Euler equations of gas dynamics, we take advantage of the fact that, while the density is discontinuous across contact waves, the pressure remains continuous there. After identifying the locations of the contact surfaces, we activate the AAAD correction in their vicinities with coefficients of order $\mathcal{O}(\Delta)$, while taking much smaller adaption coefficients elsewhere: $\mathcal{O}(\Delta^2)$ and $\mathcal{O}(\Delta^r)$ in the rest of the "rough" and "smooth" regions, respectively. Here, Δ is a spatial mesh size and r is a formal order of the underlying scheme so that the resulting AAAD method retains its formal order of accuracy in "smooth" regions.

We incorporate the proposed AAAD strategy into both second- and fifth-order schemes. First, we combine it with the second-order finite-volume (FV) central-upwind (CU) schemes developed in [25,27–29]. Second, we extend the same idea to the fifth-order finite-difference (FD) alternative weighted essentially non-oscillatory (A-WENO) framework developed in [8, 22, 33, 34, 48]. The resulting adaptive schemes are then applied to a number of 1-D and 2-D examples for the Euler equations of gas dynamics. The reported numerical results demonstrate that the proposed AAAD methods are robust and substantially less dissipative than their non-adaptive counterparts. In particular, they provide a sharper resolution of contact waves and finer structures while preserving the non-oscillatory character of the underlying schemes.

The rest of the paper is organized as follows. In §2, we briefly review the 1-D second-order CU scheme and then introduce the corresponding second-order AAAD method. We then review the 1-D fifth-order A-WENO scheme and describe the fifth-order AAAD method. In §3, we extend both the second- and fifth-order AAAD methods to the 2-D case. Finally, in §4, we present a number of 1-D and 2-D numerical

examples illustrating the performance of the proposed AAAD methods.

2. One-Dimensional Adaptive Artificial Anti-Diffusion Schemes. In this section, we consider the 1-D hyperbolic system (1.1) and present the proposed second- and fifth-order AAAD schemes. We begin with the second-order AAAD scheme based on a CU flux (§2.1) and then extend it to the fifth order via the A-WENO framework (§2.2).

2.1. One-Dimensional Second-Order Adaptive Artificial Anti-Diffusion Scheme. We first briefly review the second-order CU scheme (§2.1.1) and then describe the AAAD algorithm for the Euler equations of gas dynamics (§2.1.2).

2.1.1. One-Dimensional Second-Order Central-Upwind Scheme. Let the computational domain be partitioned into uniform cells $I_j := [x_{j-\frac12}, x_{j+\frac12}]$ of size $x_{j+\frac12} - x_{j-\frac12} \equiv \Delta x$, centered at $x_j = \big(x_{j-\frac12} + x_{j+\frac12}\big)/2$. Assume that the cell averages,

$$\overline{\boldsymbol{U}}_j(t) \approx \frac{1}{\Delta x}\int\limits_{I_j} \boldsymbol{U}(x,t)\,\mathrm{d}x,$$

are available at a certain time $t \geq 0$. In what follows, for the sake of brevity, we suppress the time dependence of indexed quantities.

Following [25], the cell averages are evolved by numerically solving the semi-discrete system

$$\frac{\mathrm{d}\overline{\boldsymbol{U}}_j}{\mathrm{d}t} = -\frac{\boldsymbol{\mathcal{F}}^{\rm FV}_{j+\frac12} - \boldsymbol{\mathcal{F}}^{\rm FV}_{j-\frac12}}{\Delta x},$$

where the CU numerical fluxes are given by

$$\boldsymbol{\mathcal{F}}^{\rm FV}_{j+\frac12} = \frac{a^+_{j+\frac12}\boldsymbol{F}(\boldsymbol{U}^-_{j+\frac12}) - a^-_{j+\frac12}\boldsymbol{F}(\boldsymbol{U}^+_{j+\frac12})}{a^+_{j+\frac12} - a^-_{j+\frac12}} + \frac{a^+_{j+\frac12}a^-_{j+\frac12}}{a^+_{j+\frac12} - a^-_{j+\frac12}}\Big(\boldsymbol{U}^+_{j+\frac12} - \boldsymbol{U}^-_{j+\frac12} - \boldsymbol{q}_{j+\frac12}\Big). \tag{2.1}$$

Here, $\boldsymbol{U}^{\pm}_{j+\frac12}$ are one-sided point values of $\boldsymbol{U}$ at the interface $x = x_{j+\frac12}$ reconstructed from the cell averages $\{\overline{\boldsymbol{U}}_j\}$ using a nonlinear limiter applied to local characteristic variables. To this end, we first introduce the matrices $\widehat{A}_{j+\frac12} = A\big(\widehat{\boldsymbol{U}}_{j+\frac12}\big)$, where $A := \frac{\partial \boldsymbol{F}}{\partial \boldsymbol{U}}$ is the Jacobian and $\widehat{\boldsymbol{U}}_{j+\frac12}$ is a certain average of $\overline{\boldsymbol{U}}_j$ and $\overline{\boldsymbol{U}}_{j+1}$, and then compute the matrices $R_{j+\frac12}$ and $\big(R_{j+\frac12}\big)^{-1}$ such that $\big(R_{j+\frac12}\big)^{-1}\widehat{A}_{j+\frac12}R_{j+\frac12}$ are diagonal. We then introduce the local characteristic variables $\boldsymbol{\Gamma}$ in the neighborhood of $x = x_{j+\frac12}$:

$$\boldsymbol{\Gamma}_\ell = \big(R_{j+\frac12}\big)^{-1}\overline{\boldsymbol{U}}_{j+\ell}, \quad \ell = -1, 0, 1, 2.$$

Equipped with the values $\boldsymbol{\Gamma}_{-1}$, $\boldsymbol{\Gamma}_0$, $\boldsymbol{\Gamma}_1$, and $\boldsymbol{\Gamma}_2$, we compute the slopes

$$(\boldsymbol{\Gamma}_x)_0 = \text{minmod}\left(\theta\,\frac{\boldsymbol{\Gamma}_0 - \boldsymbol{\Gamma}_{-1}}{\Delta x},\ \frac{\boldsymbol{\Gamma}_1 - \boldsymbol{\Gamma}_{-1}}{2\Delta x},\ \theta\,\frac{\boldsymbol{\Gamma}_1 - \boldsymbol{\Gamma}_0}{\Delta x}\right), \tag{2.2}$$

and

$$(\boldsymbol{\Gamma}_x)_1 = \text{minmod}\left(\theta\,\frac{\boldsymbol{\Gamma}_1 - \boldsymbol{\Gamma}_0}{\Delta x},\ \frac{\boldsymbol{\Gamma}_2 - \boldsymbol{\Gamma}_0}{2\Delta x},\ \theta\,\frac{\boldsymbol{\Gamma}_2 - \boldsymbol{\Gamma}_1}{\Delta x}\right). \tag{2.3}$$

Here, the minmod function, defined as

$$\text{minmod}(z_1, z_2, \ldots) := \begin{cases} \min_j\{z_j\} & \text{if } z_j > 0 \quad \forall\, j,\\ \max_j\{z_j\} & \text{if } z_j < 0 \quad \forall\, j,\\ 0 & \text{otherwise,}\end{cases}$$

is applied in the component-wise manner. The parameter $\theta \in [1, 2]$ in (2.2)–(2.3) is used to control the amount of numerical viscosity present in the resulting scheme, and larger values of θ correspond to sharper but, in general, more oscillatory reconstructions. In this paper, we take $\theta = 2$.

Equipped with (2.2) and (2.3), we evaluate

$$\mathbf{\Gamma}^-_{\frac{1}{2}} = \mathbf{\Gamma}_0 + \frac{\Delta x}{2}(\mathbf{\Gamma}_x)_0, \quad \mathbf{\Gamma}^+_{\frac{1}{2}} = \mathbf{\Gamma}_1 - \frac{\Delta x}{2}(\mathbf{\Gamma}_x)_1, \tag{2.4}$$

and then obtain the corresponding point values of $\boldsymbol{U}$ by $\boldsymbol{U}^{\pm}_{j+\frac{1}{2}} = R_{j+\frac{1}{2}}\mathbf{\Gamma}^{\pm}_{\frac{1}{2}}$.

In (2.1), $a^{\pm}_{j+\frac{1}{2}}$ are one-sided local propagation speeds, which can be estimated with the help of the smallest and largest eigenvalues of the Jacobian $A(\boldsymbol{U})$, denoted by $\lambda_1(A(\boldsymbol{U})) \le \cdots \le \lambda_d(A(\boldsymbol{U}))$. For example, one may take

$$a^+_{j+\frac{1}{2}} = \max\Big\{\lambda_d\Big(A\big(\boldsymbol{U}^-_{j+\frac{1}{2}}\big)\Big), \lambda_d\Big(A\big(\boldsymbol{U}^+_{j+\frac{1}{2}}\big)\Big), 0\Big\}, \quad a^-_{j+\frac{1}{2}} = \min\Big\{\lambda_1\Big(A\big(\boldsymbol{U}^-_{j+\frac{1}{2}}\big)\Big), \lambda_1\Big(A\big(\boldsymbol{U}^+_{j+\frac{1}{2}}\big)\Big), 0\Big\}.$$

Finally, $\boldsymbol{q}_{j+\frac{1}{2}}$ in (2.1) is the "built-in" AD term derived in [25] and given by

$$\boldsymbol{q}_{j+\frac{1}{2}} = \text{minmod}\Big(\boldsymbol{U}^+_{j+\frac{1}{2}} - \boldsymbol{U}^*_{j+\frac{1}{2}}, \boldsymbol{U}^*_{j+\frac{1}{2}} - \boldsymbol{U}^-_{j+\frac{1}{2}}\Big),$$

where

$$\boldsymbol{U}^*_{j+\frac{1}{2}} = \frac{a^+_{j+\frac{1}{2}}\boldsymbol{U}^+_{j+\frac{1}{2}} - a^-_{j+\frac{1}{2}}\boldsymbol{U}^-_{j+\frac{1}{2}} - \Big(\boldsymbol{F}\big(\boldsymbol{U}^+_{j+\frac{1}{2}}\big) - \boldsymbol{F}\big(\boldsymbol{U}^-_{j+\frac{1}{2}}\big)\Big)}{a^+_{j+\frac{1}{2}} - a^-_{j+\frac{1}{2}}}.$$

2.1.2. One-Dimensional Second-Order Adaptive Artificial Anti-Diffusion Algorithm. We now describe the proposed 1-D second-order AAAD scheme for the 1-D Euler equations of gas dynamics, which read as (1.1) with

$$\boldsymbol{U} := (\rho, \rho u, E)^\top, \quad \boldsymbol{F}(\boldsymbol{U}) := (\rho u, \rho u^2 + p, u(E+p))^\top, \tag{2.5}$$

where ρ, u, p, and E denote the density, velocity, pressure, and total energy, respectively. The system is closed by the equation of state (EOS) for ideal gases:

$$p = (\gamma - 1)\Big[E - \frac{1}{2}\rho u^2\Big], \tag{2.6}$$

where γ is the ratio of specific heats.

The Jacobian for the system (1.1), (2.5)–(2.6) is

$$A(\boldsymbol{U}) = \begin{pmatrix} 0 & 1 & 0 \\ \dfrac{\gamma-3}{2}u^2 & (3-\gamma)u & \gamma - 1 \\ -\dfrac{\gamma u E}{\rho} + (\gamma-1)u^3 & H - (\gamma-1)u^2 & \gamma u \end{pmatrix},$$

where $H = \frac{E+p}{\rho}$ is the total specific enthalpy. The eigenvalues of A are $\lambda_1 = u - c$, $\lambda_2 = u$, and $\lambda_3 = u + c$, where $c := \sqrt{\gamma p/\rho}$ is the speed of sound.

For the local linearization of $\widehat{A}_{j+\frac{1}{2}} = A\big(\widehat{\boldsymbol{U}}_{j+\frac{1}{2}}\big)$, the matrices $R_{j+\frac{1}{2}}$ and $\big(R_{j+\frac{1}{2}}\big)^{-1}$ are given by

$$R_{j+\frac{1}{2}} = \begin{pmatrix} 1 & 1 & 1 \\ \hat{u} - \hat{c} & \hat{u} & \hat{u} + \hat{c} \\ \hat{H} - \hat{u}\hat{c} & \dfrac{\hat{u}^2}{2} & \hat{H} + \hat{u}\hat{c} \end{pmatrix}, \quad \big(R_{j+\frac{1}{2}}\big)^{-1} = \frac{1}{\hat{\phi}}\begin{pmatrix} \dfrac{\hat{u}^2}{2} + \dfrac{\hat{u}\hat{\phi}}{2\hat{c}} & -\hat{u} - \dfrac{\hat{\phi}}{2\hat{c}} & 1 \\ 2\hat{\phi} - 2\hat{H} & 2\hat{u} & -2 \\ \dfrac{\hat{u}^2}{2} - \dfrac{\hat{u}\hat{\phi}}{2\hat{c}} & -\hat{u} + \dfrac{\hat{\phi}}{2\hat{c}} & 1 \end{pmatrix}.$$

Here, $\hat{(\cdot)}$ stands for the following averages:

$$\hat{\rho} = \frac{\overline{\rho}_j + \overline{\rho}_{j+1}}{2}, \quad \hat{u} = \frac{u_j + u_{j+1}}{2}, \quad \hat{p} = \frac{p_j + p_{j+1}}{2}, \quad \hat{E} = \frac{\hat{p}}{\gamma - 1} + \frac{1}{2}\hat{\rho}\hat{u}^2,$$
$$\hat{H} = \frac{\hat{E} + \hat{p}}{\hat{\rho}}, \quad \hat{\phi} = 2\hat{H} - \hat{u}^2, \quad \hat{c} = \sqrt{\gamma\hat{p}/\hat{\rho}},$$

where

$$u_j = \frac{(\overline{\rho u})_j}{\overline{\rho}_j} \quad \text{and} \quad p_j = (\gamma - 1)\left[\overline{E}_j - \frac{1}{2}\rho_j u_j^2\right].$$

Notice that all of the $\widehat{(\cdot)}$ quantities have to have a subscript index $\widehat{(\cdot)}_{j+\frac{1}{2}}$, but we have omitted it for the sake of brevity for all of the quantities except for $\widehat{A}_{j+\frac{1}{2}}$.

Our goal is to reduce the amount of numerical diffusion present in the numerical flux (2.1) by adding an AD term to it. The modified semi-discrete scheme will then read as

$$\frac{\mathrm{d}\overline{\boldsymbol{U}}_j}{\mathrm{d}t} = -\frac{\boldsymbol{\mathcal{F}}^{\mathrm{AD}}_{j+\frac{1}{2}} - \boldsymbol{\mathcal{F}}^{\mathrm{AD}}_{j-\frac{1}{2}}}{\Delta x},$$

where the numerical flux is given by

$$\boldsymbol{\mathcal{F}}^{\mathrm{AD}}_{j+\frac{1}{2}} = \boldsymbol{\mathcal{F}}^{\mathrm{FV}}_{j+\frac{1}{2}} - Q_{j+\frac{1}{2}}\frac{\overline{\boldsymbol{U}}_{j+1} - \overline{\boldsymbol{U}}_j}{\Delta x}.$$

Here, the matrix $Q_{j+\frac{1}{2}}$ is constructed to primarily add the AD into the linearly degenerate field, which corresponds to the second eigenvalue $\lambda_2 = u$. To achieve this goal, we take a diagonal AD matrix in the local characteristic space,

$$\Lambda_{j+\frac{1}{2}} := -\begin{pmatrix} 0 & 0 & 0 \\ 0 & \mathtt{C}_{j+\frac{1}{2}} & 0 \\ 0 & 0 & 0 \end{pmatrix},$$

where $\mathtt{C}_{j+\frac{1}{2}} > 0$ is yet to be chosen, and then use $Q_{j+\frac{1}{2}} = -R_{j+\frac{1}{2}}\Lambda_{j+\frac{1}{2}}\left(R_{j+\frac{1}{2}}\right)^{-1}$.

The values $\mathtt{C}_{j+\frac{1}{2}}$ are selected adaptively according to the local smoothness of the computed solution. To this end, we follow [7] and evaluate the modified minmod-based SIs. First, we compute

$$s^{\rho}_j = \frac{1}{\max\{\overline{\rho}_{j-1}, \overline{\rho}_j, \overline{\rho}_{j+1}\}}\,\mathrm{minmod}\left(\overline{\rho}_{j+1} - \overline{\rho}_j, \overline{\rho}_j - \overline{\rho}_{j-1}\right),$$

and then check whether

$$|s^{\rho}_j| > \max\left\{|s^{\rho}_{j-1}|, |s^{\rho}_{j+1}|\right\} + \varepsilon_0, \tag{2.7}$$

where ε_0 is a positive constant taken to be $\varepsilon_0 = 0.002$ as in [7]. If (2.7) is satisfied, then we mark the cells I_{j-1}, I_j, and I_{j+1} as "rough".

For those cells, at which (2.7) is satisfied, we also compute

$$s^{p}_j = \frac{1}{\max\{p_{j-1}, p_j, p_{j+1}\}}\,\mathrm{minmod}\left(p_{j+1} - p_j, p_j - p_{j-1}\right),$$

and check whether

$$|s^{p}_j| < \max\left\{|s^{p}_{j-1}|, |s^{p}_{j+1}|\right\}, \tag{2.8}$$

and if (2.8) is satisfied as well, then we mark the cells I_{j-1}, I_j, and I_{j+1} as "rough contact" cells.

Finally, the cells that are not marked as either "rough" or "rough contact" are marked as "smooth".

After all of the cells have been identified as either "rough", "rough contact", or "smooth", we select $\mathtt{C}_{j+\frac{1}{2}}$ according to Algorithm 1.

Remark 2.1. The parameter $\mathtt{C}$ is a tunable constant that should be selected for each problem at hand. In practice, we tune $\mathtt{C}$ on a coarse mesh and then use the same value on finer meshes. An example of this tuning procedure is provided in Example 4 in §4.1.

Remark 2.2. The proposed AAAD method can be extended to other hyperbolic systems of conservation laws possessing one or more linearly degenerate characteristic fields. In such cases, the AD correction can be introduced to sharpen linearly degenerate waves without affecting the genuinely nonlinear fields.

Remark 2.3. We stress that the proposed AAAD methodology is not restricted to the CU schemes and can be used with other stable numerical fluxes.

Algorithm 1 Assignment of $\mathtt{C}_{j+\frac12}$

for each cell interface $x = x_{j+\frac12}$ **do**
  if either I_j or I_{j+1} is a "rough contact" cell **then**
    set $\mathtt{C}_{j+\frac12} = \mathtt{C}\,\Delta x$
  else
    set $\mathtt{C}_{j+\frac12} = \mathtt{C}\,(\Delta x)^2$
  end if
end for

2.2. One-Dimensional Fifth-Order Adaptive Artificial Anti-Diffusion Scheme. We now construct a fifth-order AAAD scheme. As in the second-order scheme, we first briefly review the fifth-order A-WENO scheme (§2.2.1) and then introduce the fifth-order adaptive algorithm (§2.2.2).

2.2.1. One-Dimensional Fifth-Order A-WENO Scheme. Following [22], the point values $\boldsymbol{U}_j$ are evolved in time by numerically solving

$$\frac{\mathrm{d}\boldsymbol{U}_j}{\mathrm{d}t} = -\frac{\boldsymbol{\mathcal{H}}_{j+\frac12} - \boldsymbol{\mathcal{H}}_{j-\frac12}}{\Delta x},$$

where the fifth-order numerical flux is

$$\boldsymbol{\mathcal{H}}_{j+\frac12} = \boldsymbol{\mathcal{F}}^{\mathrm{FV}}_{j+\frac12} - \frac{1}{24}(\Delta x)^2(\boldsymbol{F}_{xx})_{j+\frac12} + \frac{7}{5760}(\Delta x)^4(\boldsymbol{F}_{xxxx})_{j+\frac12}.$$

Here, $\boldsymbol{\mathcal{F}}^{\mathrm{FV}}_{j+\frac12}$ is a FV numerical flux (we use the CU flux given by (2.1)), and $(\boldsymbol{F}_{xx})_{j+\frac12}$ and $(\boldsymbol{F}_{xxxx})_{j+\frac12}$ are higher-order correction terms computed using fourth- and second-order finite differences, respectively:

$$(\boldsymbol{F}_{xx})_{j+\frac12} = \frac{1}{48(\Delta x)^2}\Big[-5\boldsymbol{F}_{j-2} + 39\boldsymbol{F}_{j-1} - 34\boldsymbol{F}_j - 34\boldsymbol{F}_{j+1} + 39\boldsymbol{F}_{j+2} - 5\boldsymbol{F}_{j+3}\Big],$$
$$(\boldsymbol{F}_{xxxx})_{j+\frac12} = \frac{1}{2(\Delta x)^4}\Big[\boldsymbol{F}_{j-2} - 3\boldsymbol{F}_{j-1} + 2\boldsymbol{F}_j + 2\boldsymbol{F}_{j+1} - 3\boldsymbol{F}_{j+2} + \boldsymbol{F}_{j+3}\Big],$$

where $\boldsymbol{F}_j := \boldsymbol{F}(\boldsymbol{U}_j)$.

The one-sided point values $\boldsymbol{U}^{\pm}_{j+\frac12}$, which are required in (2.1), must be reconstructed with at least fifth order of accuracy. We employ the fifth-order WENO-Z interpolation [22,33] applied to local characteristic variables; see Appendix A for details.

2.2.2. One-Dimensional Fifth-Order Adaptive Artificial Anti-Diffusion Algorithm. The fifth-order adaptive scheme is defined in an analogous manner. We consider

$$\frac{\mathrm{d}\boldsymbol{U}_j}{\mathrm{d}t} = -\frac{\boldsymbol{\mathcal{H}}^{\mathrm{AD}}_{j+\frac12} - \boldsymbol{\mathcal{H}}^{\mathrm{AD}}_{j-\frac12}}{\Delta x},$$

where the adaptive numerical flux is

$$\boldsymbol{\mathcal{H}}^{\mathrm{AD}}_{j+\frac12} = \boldsymbol{\mathcal{H}}_{j+\frac12} - Q_{j+\frac12}\frac{\boldsymbol{U}_{j+1} - \boldsymbol{U}_j}{\Delta x},$$

and the matrix $Q_{j+\frac12}$ is defined as in the second-order AAAD scheme (see §2.1.2) but with the values of $\mathtt{C}_{j+\frac12}$ determined according to Algorithm 2.

As in the second-order case, this choice ensures that the added AD term does not affect the designed order of accuracy in "smooth" regions, while enhancing the resolution of linearly degenerate waves.

3. Two-Dimensional Adaptive Artificial Anti-Diffusion Schemes. In this section, we consider the 2-D hyperbolic system (1.2) and introduce the proposed AAAD methods for the 2-D Euler equations of gas dynamics, which read as (1.2) with $\boldsymbol{U} = (\rho, \rho u, \rho v, E)^\top$, $\boldsymbol{F} = \big(\rho u, \rho u^2 + p, \rho uv, u(E+p)\big)^\top$, and

Algorithm 2 Assignment of $\mathtt{C}_{j+\frac{1}{2}}$

for each cell interface $x = x_{j+\frac{1}{2}}$ **do**
  if either I_j or I_{j+1} is a "rough contact" cell **then**
    set $\mathtt{C}_{j+\frac{1}{2}} = \mathtt{C}\,\Delta x$
  else if either I_j or I_{j+1} is a "rough" cell **then**
    set $\mathtt{C}_{j+\frac{1}{2}} = \mathtt{C}\,(\Delta x)^2$
  else
    set $\mathtt{C}_{j+\frac{1}{2}} = \mathtt{C}\,(\Delta x)^5$
  end if
end for

$\boldsymbol{G} = \big(\rho v, \rho uv, \rho v^2 + p, v(E+p)\big)^\top$. Here, u and v are the x- and y-directional velocities, respectively, and the pressure is given by the ideal-gas EOS

$$p = (\gamma - 1)\Big[E - \frac{\rho}{2}(u^2 + v^2)\Big].$$

3.1. Two-Dimensional Second-Order Adaptive Artificial Anti-Diffusion Scheme. Let the computational domain be partitioned into uniform cells $I_{j,k} := [x_{j-\frac{1}{2}}, x_{j+\frac{1}{2}}] \times [y_{k-\frac{1}{2}}, y_{k+\frac{1}{2}}]$, centered at $(x_j, y_k) = \big((x_{j-\frac{1}{2}} + x_{j+\frac{1}{2}})/2, (y_{k-\frac{1}{2}} + y_{k+\frac{1}{2}})/2\big)$, with $x_{j+\frac{1}{2}} - x_{j-\frac{1}{2}} \equiv \Delta x$ and $y_{k+\frac{1}{2}} - y_{k-\frac{1}{2}} \equiv \Delta y$.

Assume that the computed cell averages,

$$\overline{\boldsymbol{U}}_{j,k} \approx \frac{1}{\Delta x \Delta y} \int\limits_{I_{j,k}} \boldsymbol{U}(x, y, t)\,\mathrm{d}x\,\mathrm{d}y,$$

are available at a certain time level $t \geq 0$. They are evolved by numerically solving the following semi-discrete system:

$$\frac{\mathrm{d}\overline{\boldsymbol{U}}_{j,k}}{\mathrm{d}t} = -\frac{\boldsymbol{\mathcal{F}}^{\mathrm{AD}}_{j+\frac{1}{2},k} - \boldsymbol{\mathcal{F}}^{\mathrm{AD}}_{j-\frac{1}{2},k}}{\Delta x} - \frac{\boldsymbol{\mathcal{G}}^{\mathrm{AD}}_{j,k+\frac{1}{2}} - \boldsymbol{\mathcal{G}}^{\mathrm{AD}}_{j,k-\frac{1}{2}}}{\Delta y},$$

where the adaptive numerical fluxes are defined by

$$\boldsymbol{\mathcal{F}}^{\mathrm{AD}}_{j+\frac{1}{2},k} = \boldsymbol{\mathcal{F}}^{\mathrm{FV}}_{j+\frac{1}{2},k} - Q_{j+\frac{1}{2},k}\frac{\overline{\boldsymbol{U}}_{j+1,k} - \overline{\boldsymbol{U}}_{j,k}}{\Delta x}, \qquad \boldsymbol{\mathcal{G}}^{\mathrm{AD}}_{j,k+\frac{1}{2}} = \boldsymbol{\mathcal{G}}^{\mathrm{FV}}_{j,k+\frac{1}{2}} - Q_{j,k+\frac{1}{2}}\frac{\overline{\boldsymbol{U}}_{j,k+1} - \overline{\boldsymbol{U}}_{j,k}}{\Delta y}.$$

Here, $\boldsymbol{\mathcal{F}}^{\mathrm{FV}}_{j+\frac{1}{2},k}$ and $\boldsymbol{\mathcal{G}}^{\mathrm{FV}}_{j,k+\frac{1}{2}}$ are the CU numerical fluxes from [6, 25]

(3.1)

$$\boldsymbol{\mathcal{F}}^{\mathrm{FV}}_{j+\frac{1}{2},k} = \frac{a^+_{j+\frac{1}{2},k}\boldsymbol{F}\big(\boldsymbol{U}^-_{j+\frac{1}{2},k}\big) - a^-_{j+\frac{1}{2},k}\boldsymbol{F}\big(\boldsymbol{U}^+_{j+\frac{1}{2},k}\big)}{a^+_{j+\frac{1}{2},k} - a^-_{j+\frac{1}{2},k}} + \frac{a^+_{j+\frac{1}{2},k}a^-_{j+\frac{1}{2},k}}{a^+_{j+\frac{1}{2},k} - a^-_{j+\frac{1}{2},k}}\Big(\boldsymbol{U}^+_{j+\frac{1}{2},k} - \boldsymbol{U}^-_{j+\frac{1}{2},k} - \boldsymbol{q}^x_{j+\frac{1}{2},k}\Big),$$

$$\boldsymbol{\mathcal{G}}^{\mathrm{FV}}_{j,k+\frac{1}{2}} = \frac{b^+_{j,k+\frac{1}{2}}\boldsymbol{G}\big(\boldsymbol{U}^-_{j,k+\frac{1}{2}}\big) - b^-_{j,k+\frac{1}{2}}\boldsymbol{G}\big(\boldsymbol{U}^+_{j,k+\frac{1}{2}}\big)}{b^+_{j,k+\frac{1}{2}} - b^-_{j,k+\frac{1}{2}}} + \frac{b^+_{j,k+\frac{1}{2}}b^-_{j,k+\frac{1}{2}}}{b^+_{j,k+\frac{1}{2}} - b^-_{j,k+\frac{1}{2}}}\Big(\boldsymbol{U}^+_{j,k+\frac{1}{2}} - \boldsymbol{U}^-_{j,k+\frac{1}{2}} - \boldsymbol{q}^y_{j,k+\frac{1}{2}}\Big).$$

The one-sided interface point values $\boldsymbol{U}^\pm_{j+\frac{1}{2},k}$ and $\boldsymbol{U}^\pm_{j,k+\frac{1}{2}}$ are obtained at the points $(x, y) = (x_{j+\frac{1}{2}}, y_k)$ and $(x, y) = (x_j, y_{k+\frac{1}{2}})$, respectively using a piecewise linear reconstruction applied to the local characteristic variables in the following manner. We will only show how to compute the point values $\boldsymbol{U}^\pm_{j+\frac{1}{2},k}$, as $\boldsymbol{U}^\pm_{j,k+\frac{1}{2}}$ can be derived in a similar way. As in the 1-D case, we first introduce the matrices $\widehat{A}_{j+\frac{1}{2},k} = A\big(\widehat{\boldsymbol{U}}_{j+\frac{1}{2},k}\big)$, where $A(\boldsymbol{U}) = \frac{\partial \boldsymbol{F}}{\partial \boldsymbol{U}}$ is, as before, the Jacobian and $\widehat{\boldsymbol{U}}_{j+\frac{1}{2},k}$ is a certain average of $\overline{\boldsymbol{U}}_{j,k}$ and $\overline{\boldsymbol{U}}_{j+1,k}$, and then compute the matrices $R_{j+\frac{1}{2},k}$ and $\big(R_{j+\frac{1}{2},k}\big)^{-1}$ such that $\big(R_{j+\frac{1}{2},k}\big)^{-1}\widehat{A}_{j+\frac{1}{2},k}R_{j+\frac{1}{2},k}$ are diagonal. We then introduce the local characteristic variables $\boldsymbol{\Gamma}$ in the neighborhood of $(x, y) = (x_{j+\frac{1}{2}}, y_k)$:

$$\boldsymbol{\Gamma}_\ell = \big(R_{j+\frac{1}{2},k}\big)^{-1}\overline{\boldsymbol{U}}_{j+\ell,k}, \quad \ell = -1, 0, 1, 2.$$

Equipped with the values $\mathbf{\Gamma}_{-1}$, $\mathbf{\Gamma}_0$, $\mathbf{\Gamma}_1$, and $\mathbf{\Gamma}_2$, we compute $\mathbf{\Gamma}^{\pm}_{\frac12}$ precisely as in (2.2)–(2.4), and then

$$\boldsymbol{U}^{\pm}_{j+\frac12,k}=R_{j+\frac12,k}\mathbf{\Gamma}^{\pm}_{\frac12}.$$

Remark 3.1. The matrices $R_{j+\frac12,k}$ and $\big(R_{j+\frac12,k}\big)^{-1}$ for the 2-D Euler equations of gas dynamics can be found in [4, Appendix C].

The one-sided local propagation speeds $a^{\pm}_{j+\frac12,k}$ and $b^{\pm}_{j,k+\frac12}$ can be estimated using the smallest and largest eigenvalues of the Jacobians $A(\boldsymbol{U})$ and $B(\boldsymbol{U}):=\frac{\partial \boldsymbol{G}}{\partial \boldsymbol{U}}$. We set

$$a^+_{j+\frac12,k}=\max\Big\{\lambda_d\big(A(\boldsymbol{U}^-_{j+\frac12,k})\big),\lambda_d\big(A(\boldsymbol{U}^+_{j+\frac12,k})\big),0\Big\},\quad a^-_{j+\frac12,k}=\min\Big\{\lambda_1\big(A(\boldsymbol{U}^-_{j+\frac12,k})\big),\lambda_1\big(A(\boldsymbol{U}^+_{j+\frac12,k})\big),0\Big\},$$
$$b^+_{j,k+\frac12}=\max\Big\{\lambda_d\big(B(\boldsymbol{U}^-_{j,k+\frac12})\big),\lambda_d\big(B(\boldsymbol{U}^+_{j,k+\frac12})\big),0\Big\},\quad b^-_{j,k+\frac12}=\min\Big\{\lambda_1\big(B(\boldsymbol{U}^-_{j,k+\frac12})\big),\lambda_1\big(B(\boldsymbol{U}^+_{j,k+\frac12})\big),0\Big\}.$$

The "built-in" AD terms $\boldsymbol{q}^x_{j+\frac12,k}$ and $\boldsymbol{q}^y_{j,k+\frac12}$ are defined as in [6]:

$$\boldsymbol{q}^x_{j+\frac12,k}=\text{minmod}\Big(\boldsymbol{U}^+_{j+\frac12,k}-\boldsymbol{U}^*_{j+\frac12,k},\boldsymbol{U}^*_{j+\frac12,k}-\boldsymbol{U}^-_{j+\frac12,k}\Big),$$
$$\boldsymbol{q}^y_{j,k+\frac12}=\text{minmod}\Big(\boldsymbol{U}^+_{j,k+\frac12}-\boldsymbol{U}^*_{j,k+\frac12},\boldsymbol{U}^*_{j,k+\frac12}-\boldsymbol{U}^-_{j,k+\frac12}\Big),$$

where

$$\boldsymbol{U}^*_{j+\frac12,k}=\frac{a^+_{j+\frac12,k}\boldsymbol{U}^+_{j+\frac12,k}-a^-_{j+\frac12,k}\boldsymbol{U}^-_{j+\frac12,k}-\Big(\boldsymbol{F}\big(\boldsymbol{U}^+_{j+\frac12,k}\big)-\boldsymbol{F}\big(\boldsymbol{U}^-_{j+\frac12,k}\big)\Big)}{a^+_{j+\frac12,k}-a^-_{j+\frac12,k}},$$
$$\boldsymbol{U}^*_{j,k+\frac12}=\frac{b^+_{j,k+\frac12}\boldsymbol{U}^+_{j,k+\frac12}-b^-_{j,k+\frac12}\boldsymbol{U}^-_{j,k+\frac12}-\Big(\boldsymbol{G}\big(\boldsymbol{U}^+_{j,k+\frac12}\big)-\boldsymbol{G}\big(\boldsymbol{U}^-_{j,k+\frac12}\big)\Big)}{b^+_{j,k+\frac12}-b^-_{j,k+\frac12}}.$$

For the 2-D Euler equations of gas dynamics, the eigenvalues of Jacobians $A(\boldsymbol{U})$ and $B(\boldsymbol{U})$ are

$$\lambda_1(A(\boldsymbol{U}))=u-c,\quad \lambda_2(A(\boldsymbol{U}))=\lambda_3(A(\boldsymbol{U}))=u,\quad \lambda_4(A(\boldsymbol{U}))=u+c,$$
$$\lambda_1(B(\boldsymbol{U}))=v-c,\quad \lambda_2(B(\boldsymbol{U}))=\lambda_3(B(\boldsymbol{U}))=v,\quad \lambda_4(B(\boldsymbol{U}))=v+c.$$

As in the 1-D case, we add the AD terms to the linearly degenerate fields only. Specifically, we take $Q_{j+\frac12,k}=-R_{j+\frac12,k}\Lambda_{j+\frac12,k}\big(R_{j+\frac12,k}\big)^{-1}$ and $Q_{j,k+\frac12}=-R_{j,k+\frac12}\Lambda_{j,k+\frac12}\big(R_{j,k+\frac12}\big)^{-1}$, where

$$\Lambda_{j+\frac12,k}:=\begin{pmatrix}0&0&0&0\\0&\mathtt{C}_{j+\frac12,k}&0&0\\0&0&\mathtt{C}_{j+\frac12,k}&0\\0&0&0&0\end{pmatrix},\quad \Lambda_{j,k+\frac12}:=\begin{pmatrix}0&0&0&0\\0&\mathtt{C}_{j,k+\frac12}&0&0\\0&0&\mathtt{C}_{j,k+\frac12}&0\\0&0&0&0\end{pmatrix}.$$

The values of $\mathtt{C}_{j+\frac12,k}$ and $\mathtt{C}_{j,k+\frac12}$ are selected adaptively according to the local smoothness of the computed solution. To this end, we follow [7] and evaluate modified minmod-based SIs for ρ and p in a dimension-by-dimension manner. We now show how to check the local smoothness of the computed solution and to determine the values of $\mathtt{C}_{j+\frac12,k}$ in the x-direction. (The values of $\mathtt{C}_{j,k+\frac12}$ can be obtained similarly, and we omit the details for the sake of brevity.)

We first compute the x-directional SIs:

$$s^{x,\rho}_{j,k}=\frac{1}{\max\{\overline{\rho}_{j-1,k},\overline{\rho}_{j,k},\overline{\rho}_{j+1,k}\}}\,\text{minmod}\left(\overline{\rho}_{j+1,k}-\overline{\rho}_{j,k},\overline{\rho}_{j,k}-\overline{\rho}_{j-1,k}\right),$$

and then check whether

$$|s^{x,\rho}_{j,k}|>\max\left\{|s^{x,\rho}_{j-1,k}|,|s^{x,\rho}_{j+1,k}|\right\}+\varepsilon_0, \tag{3.2}$$

where ε_0 is a positive constant taken to be $\varepsilon_0 = 0.002$ as in the 1-D case. If (3.2) is satisfied, then we mark the cells $I_{j-1,k}$, $I_{j,k}$, and $I_{j+1,k}$ as "rough".

For those cells, at which (3.2) is satisfied, we also compute the SIs:

$$s^{x,p}_{j,k} = \frac{1}{\max\{p_{j-1,k}, p_{j,k}, p_{j+1,k}\}} \operatorname{minmod}\left(p_{j+1,k} - p_{j,k}, p_{j,k} - p_{j-1,k}\right),$$

and check whether

$$|s^{x,p}_{j,k}| < \max\left\{|s^{x,p}_{j-1,k}|, |s^{x,p}_{j+1,k}|\right\}, \tag{3.3}$$

and if (3.3) is satisfied as well, then we mark the cells $I_{j-1,k}$, $I_{j,k}$, and $I_{j+1,k}$ as "rough contact" cells.

Finally, the cells that are not marked as either "rough" or "rough contact" are marked as "smooth".

After all of the cells have been identified as either "rough", "rough contact", or "smooth", we select $\mathtt{C}_{j+\frac12,k}$ according to Algorithm 3.

Algorithm 3 Assignment of $\mathtt{C}_{j+\frac12,k}$

for each $(x_{j+\frac12}, y_k)$ **do**
  if either $I_{j,k}$ or $I_{j+1,k}$ is a "rough contact" cell **then**
    set $\mathtt{C}_{j+\frac12,k} = \mathtt{C}\,\Delta x$
  else
    set $\mathtt{C}_{j+\frac12,k} = \mathtt{C}\,(\Delta x)^2$
  end if
end for

Remark 3.2. As in the 1-D case, $\mathtt{C}$ is a positive tunable constant to be selected for each problem at hand. In practice, one may tune $\mathtt{C}$ on a coarse mesh and then use the same value on finer meshes, as demonstrated in Example 9 in §4.2.

3.2. Two-Dimensional Fifth-Order Adaptive Artificial Anti-Diffusion Scheme. We now extend the 2-D second-order AAAD method to the fifth order of accuracy via the framework of the A-WENO scheme. Assume that point values $\boldsymbol{U}_{j,k} \approx \boldsymbol{U}(x_j, y_k, t)$ are available at a time level t. They are evolved in time by numerically solving

$$\frac{\mathrm{d}\boldsymbol{U}_{j,k}}{\mathrm{d}t} = -\frac{\boldsymbol{\mathcal{H}}^{\rm AD}_{j+\frac12,k} - \boldsymbol{\mathcal{H}}^{\rm AD}_{j-\frac12,k}}{\Delta x} - \frac{\boldsymbol{\mathcal{H}}^{\rm AD}_{j,k+\frac12} - \boldsymbol{\mathcal{H}}^{\rm AD}_{j,k-\frac12}}{\Delta y},$$

where the numerical fluxes are defined by

$$\begin{aligned}
\boldsymbol{\mathcal{H}}^{\rm AD}_{j+\frac12,k} &= \boldsymbol{\mathcal{F}}^{\rm FV}_{j+\frac12,k} - \frac{1}{24}(\Delta x)^2(\boldsymbol{F}_{xx})_{j+\frac12,k} + \frac{7}{5760}(\Delta x)^4(\boldsymbol{F}_{xxxx})_{j+\frac12,k} - Q_{j+\frac12,k}\,\frac{\boldsymbol{U}_{j+1,k} - \boldsymbol{U}_{j,k}}{\Delta x},\\
\boldsymbol{\mathcal{H}}^{\rm AD}_{j,k+\frac12} &= \boldsymbol{\mathcal{G}}^{\rm FV}_{j,k+\frac12} - \frac{1}{24}(\Delta y)^2(\boldsymbol{G}_{yy})_{j,k+\frac12} + \frac{7}{5760}(\Delta y)^4(\boldsymbol{G}_{yyyy})_{j,k+\frac12} - Q_{j,k+\frac12}\,\frac{\boldsymbol{U}_{j,k+1} - \boldsymbol{U}_{j,k}}{\Delta y}.
\end{aligned} \tag{3.4}$$

Here, $\boldsymbol{\mathcal{F}}^{\rm FV}_{j+\frac12,k}$ and $\boldsymbol{\mathcal{G}}^{\rm FV}_{j,k+\frac12}$ are the CU fluxes defined in (3.1), and the higher-order correction terms are computed by fourth- and second-order finite differences, respectively:

$$\begin{aligned}
(\boldsymbol{F}_{xx})_{j+\frac12,k} &= \frac{1}{48(\Delta x)^2}\Big(-5\boldsymbol{F}_{j-2,k} + 39\boldsymbol{F}_{j-1,k} - 34\boldsymbol{F}_{j,k} - 34\boldsymbol{F}_{j+1,k} + 39\boldsymbol{F}_{j+2,k} - 5\boldsymbol{F}_{j+3,k}\Big),\\
(\boldsymbol{F}_{xxxx})_{j+\frac12,k} &= \frac{1}{2(\Delta x)^4}\Big(\boldsymbol{F}_{j-2,k} - 3\boldsymbol{F}_{j-1,k} + 2\boldsymbol{F}_{j,k} + 2\boldsymbol{F}_{j+1,k} - 3\boldsymbol{F}_{j+2,k} + \boldsymbol{F}_{j+3,k}\Big),\\
(\boldsymbol{G}_{yy})_{j,k+\frac12} &= \frac{1}{48(\Delta y)^2}\Big(-5\boldsymbol{G}_{j,k-2} + 39\boldsymbol{G}_{j,k-1} - 34\boldsymbol{G}_{j,k} - 34\boldsymbol{G}_{j,k+1} + 39\boldsymbol{G}_{j,k+2} - 5\boldsymbol{G}_{j,k+3}\Big),\\
(\boldsymbol{G}_{yyyy})_{j,k+\frac12} &= \frac{1}{2(\Delta y)^4}\Big(\boldsymbol{G}_{j,k-2} - 3\boldsymbol{G}_{j,k-1} + 2\boldsymbol{G}_{j,k} + 2\boldsymbol{G}_{j,k+1} - 3\boldsymbol{G}_{j,k+2} + \boldsymbol{G}_{j,k+3}\Big),
\end{aligned}$$

Algorithm 4 Assignment of $\mathtt{C}_{j+\frac{1}{2},k}$

for each $(x_{j+\frac{1}{2}}, y_k)$ **do**
  if either $I_{j,k}$ or $I_{j+1,k}$ is a "rough contact" cell **then**
    set $\mathtt{C}_{j+\frac{1}{2},k} = \mathtt{C}\,\Delta x$
  else if either $I_{j,k}$ or $I_{j+1,k}$ is a "rough" cell **then**
    set $\mathtt{C}_{j+\frac{1}{2},k} = \mathtt{C}\,(\Delta x)^2$
  else
    set $\mathtt{C}_{j+\frac{1}{2},k} = \mathtt{C}\,(\Delta x)^5$
  end if
end for

where $\boldsymbol{F}_{j,k} := \boldsymbol{F}(\boldsymbol{U}_{j,k})$ and $\boldsymbol{G}_{j,k} := \boldsymbol{G}(\boldsymbol{U}_{j,k})$.

The matrix $Q_{j+\frac{1}{2},k}$ is defined as in the second-order AAAD scheme (see §3.1) but with the values of $\mathtt{C}_{j+\frac{1}{2},k}$ determined according to Algorithm 4.

The matrix $Q_{j,k+\frac{1}{2}}$ can be obtained similarly, and we omit the details for the sake of brevity.

Finally, to ensure the fifth order of accuracy, the one-sided interface values $\boldsymbol{U}^{\pm}_{j+\frac{1}{2},k}$ and $\boldsymbol{U}^{\pm}_{j,k+\frac{1}{2}}$ are approximated using a 1-D fifth-order WENO-Z interpolation applied to local characteristic variables in the x- and y-directions, respectively.

4. Numerical Examples. In this section, we test the proposed AAAD schemes on a series of benchmark problems and compare their performance with that of the corresponding second-order CU and fifth-order A-WENO schemes. For the sake of brevity, we refer to the second- and fifth-order AAAD schemes as AAAD2 and AAAD5, respectively.

We numerically integrate the semi-discrete systems by the three-stage third-order strong stability preserving Runge-Kutta (SSP RK3) method (see, e.g., [15,16]) and use the CFL number 0.4.

4.1. One-Dimensional Examples. We begin with the 1-D Euler equations of gas dynamics, in which we take $\gamma = 1.4$.

Example 1—1-D Accuracy Test. In the first example taken from [24], we consider the following smooth initial data:

$$u(x,0) = \sin\Big(\frac{\pi x}{5} + \frac{\pi}{4}\Big), \quad \rho(x,0) = \left[\frac{\gamma-1}{2\sqrt{\gamma}}\Big(u(x,0)+10\Big)\right]^{\frac{2}{\gamma-1}}, \quad p(x,0) = \rho^{\gamma}(x,0),$$

subject to the periodic boundary conditions in the computational domain $[0,10]$. We compute the numerical solution until the final time $t = 0.1$ by the studied AAAD2 and AAAD5 schemes (both with the adaptation constant $\mathtt{C} = 0.1$) on a sequence of uniform meshes with $\Delta x = 1/20$, $1/40$, $1/80$, $1/160$, and $1/320$.

We then compute the L^1-errors and estimate the experimental convergence rates using the following Runge formulas based on the solutions computed on three consecutive uniform grids with mesh sizes Δx, $2\Delta x$, and $4\Delta x$, denoted by $(\cdot)^{\Delta x}$, $(\cdot)^{2\Delta x}$, and $(\cdot)^{4\Delta x}$, respectively:

$$\text{Error}(\Delta x) \approx \frac{\delta_{12}^2}{|\delta_{12}-\delta_{24}|}, \quad \text{Rate}(\Delta x) \approx \log_2\left(\frac{\delta_{24}}{\delta_{12}}\right),$$

where $\delta_{12} := \|(\cdot)^{\Delta x} - (\cdot)^{2\Delta x}\|_{L^1}$ and $\delta_{24} := \|(\cdot)^{2\Delta x} - (\cdot)^{4\Delta x}\|_{L^1}$. The obtained results are reported in Table 4.1, where one can clearly observe the expected second- and fifth-order accuracy of the AAAD2 and AAAD5 schemes, respectively.

Remark 4.1. We stress that, in order to achieve the fifth order of accuracy for the AAAD5 scheme, we use smaller time steps with $\Delta t \sim (\Delta x)^{5/3}$ in order to balance the spatial and temporal errors.

Δx	AAAD2		AAAD5	
	Error	Rate	Error	Rate
1/80	1.11e-04	2.05	1.24e-08	4.80
1/160	2.32e-05	2.14	2.81e-10	5.12
1/320	6.33e-06	2.03	9.81e-12	4.98

TABLE 4.1
Example 1: The L^1-errors of the density ρ and experimental convergence rates for the AAAD schemes.

Example 2—Titarev-Toro Problem. In the second 1-D example, we consider the shock-entropy wave interaction problem taken from [44]; see also [41, 45]. The initial conditions,

$$(\rho,u,p)(x,0)=\begin{cases}(1.51695,0.523346,1.805), & x<-4.5,\\ (1+0.1\sin(20x),0,1), & x>-4.5,\end{cases}$$

correspond to a forward-facing shock wave of Mach 1.1 interacting with high-frequency density perturbations. In this example, the computational domain is $[-5,5]$ and we impose the free boundary conditions.

We first compute the numerical solution until the final time $t=5$ by the studied AAAD2 (with the adaptation constant $\mathtt{C}=0.04$) on a uniform mesh with $\Delta x=1/80$ and in Figure 4.1, we plot the obtained density along with the reference one computed by the CU scheme on a much finer mesh with $\Delta x=1/800$. As one can see, the AAAD2 scheme produces much more accurate results than the CU scheme. We then repeat this computation using the AAAD5 scheme (with the adaptation constant $\mathtt{C}=0.003$), but on a coarser uniform mesh with $\Delta x=1/40$. The obtained numerical results, shown in Figure 4.2, demonstrate that the fifth-order solution also substantially improves when the AAAD terms are added. We stress that the fifth-order computations were run on a coarser mesh since finer mesh results were close to the reference solution.

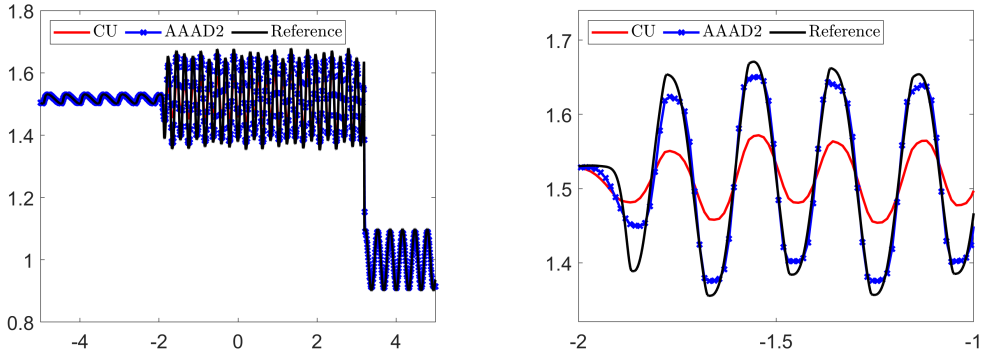

FIG. 4.1. Example 2: Density ρ computed by the CU and AAAD2 schemes on a uniform mesh with $\Delta x=1/80$ (left) and zoom at $x\in[-2,-1]$ (right).

Example 3—Shock-Density Wave Interaction. In this example taken from [42], we consider the shock-density wave interaction problem with the initial data,

$$(\rho,u,p)(x,0)=\begin{cases}\left(\dfrac{27}{7},\dfrac{4\sqrt{35}}{9},\dfrac{31}{3}\right), & x<-4,\\ (1+0.2\sin(5x),0,1), & x>-4,\end{cases}$$

prescribed in the computational domain $[-5,15]$ with the free boundary conditions.

We compute the numerical solutions until the final time $t=5$ by the studied AAAD2 scheme (with the adaptation constant $\mathtt{C}=0.1$) on a uniform mesh with $\Delta x=1/80$ and AAAD5 scheme (with the adaptation constant $\mathtt{C}=0.03$) on a coarser uniform mesh with $\Delta x=1/20$. We present the results in

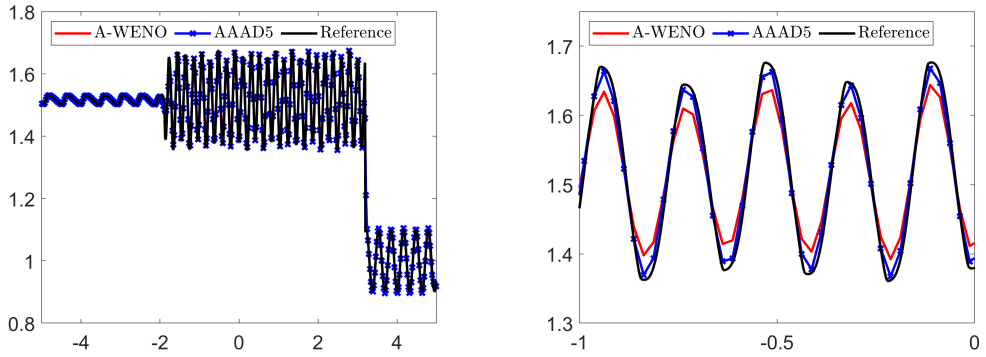

FIG. 4.2. Example 2: Density ρ computed by the A-WENO and AAAD5 schemes on a uniform mesh with $\Delta x = 1/40$ (left), which is coarser than the mesh used in Figure 4.1, and zoom at $x \in [-1, 0]$ (right).

Figures 4.3–4.4 together with a reference solution computed by the CU scheme on a much finer mesh with $\Delta x = 1/400$. One can see that the AAAD2 and AAAD5 schemes yield substantially improved resolution compared with their CU and A-WENO counterparts.

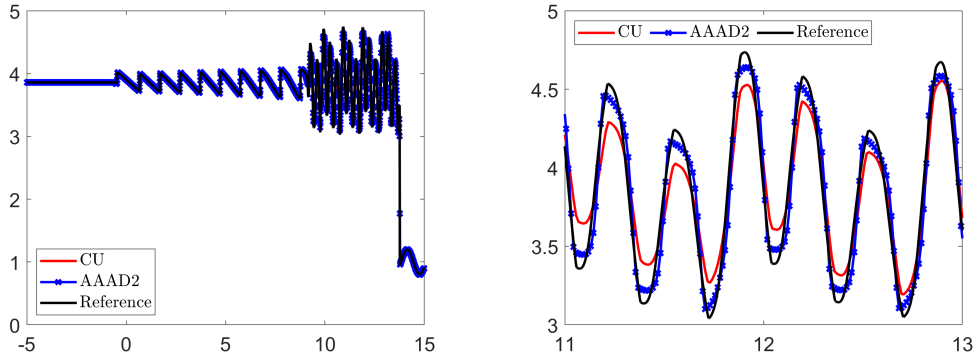

FIG. 4.3. Example 3: Density ρ computed by the CU and AAAD2 schemes on a uniform mesh with $\Delta x = 1/80$ (left) and zoom at $x \in [11, 13]$ (right).

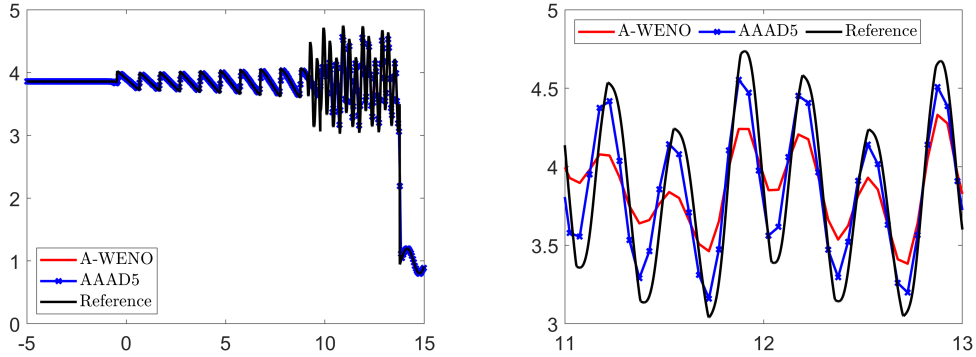

FIG. 4.4. Example 3: Density ρ computed by the A-WENO and AAAD5 schemes on a uniform mesh with $\Delta x = 1/20$ (left), which is much coarser than the mesh used in Figure 4.3, and zoom at $x \in [11, 13]$ (right).

Example 4—Shock-Bubble Interaction. In the fourth example taken from [30], we consider the shock-bubble interaction problem with the initial data

$$(\rho,u,p)(x,0)=\begin{cases}(13.1538,0,1), & \text{if } |x|<0.25,\\ (1.3333,-0.3535,1.5), & \text{if } x>0.75,\\ (1,0,1), & \text{otherwise,}\end{cases}$$

which correspond to a left-moving shock initially located at $x=0.75$ and a bubble of radius 0.25 initially located at the origin. We impose the solid wall boundary conditions on the left and free boundary conditions on the right of the computational domain $[-1,1]$.

We compute the numerical solution until the final time $t=3$ by the studied AAAD2 (with the adaptation constant $\mathtt{C}=0.15$) and AAAD5 (with the adaptation constant $\mathtt{C}=0.05$) schemes on a uniform mesh with $\Delta x=1/100$. The obtained results are presented in Figures 4.5–4.6 along with a reference solution computed by the CU scheme on a much finer mesh with $\Delta x=1/2000$. One can see that both AAAD2 and AAAD5 achieve improved resolution of the contact discontinuities.

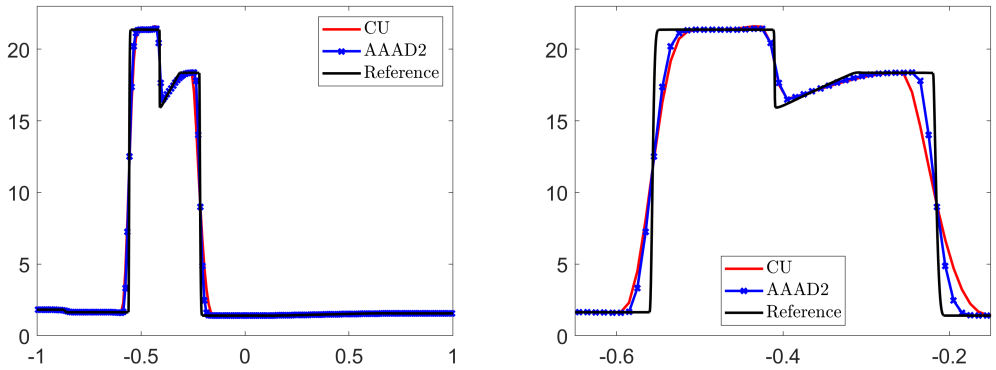

FIG. 4.5. Example 4: Density ρ computed by the CU and AAAD2 schemes (left) and zoom at $x\in[-0.65,-0.15]$ (right).

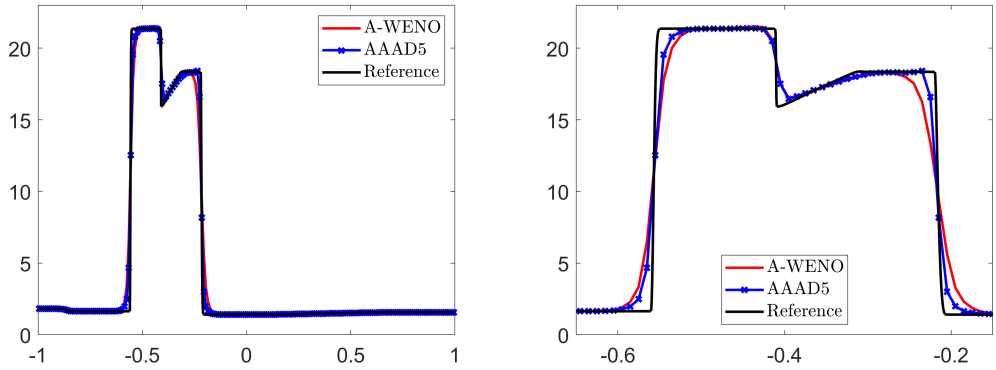

FIG. 4.6. Example 4: Density ρ computed by the A-WENO and AAAD5 schemes (left) and zoom at $x\in[-0.65,-0.15]$ (right).

We use this example to demonstrate the adaption coefficient tuning procedure. To this end, we first adjust $\mathtt{C}$ on a coarse mesh (so that the tuning process is computationally inexpensive) and then use the selected value for high-resolution computations on finer meshes. We compute the numerical solutions by the AAAD2 scheme on a coarse mesh with $\Delta x=1/100$ using $\mathtt{C}=0.05$, 0.15, and 0.25, and present the results in Figure 4.7 (left), where one can see that $\mathtt{C}=0.15$ seems to be a reasonable choice as the larger value $\mathtt{C}=0.25$ produces a small oscillation. We then take $\mathtt{C}=0.15$, compute the corresponding numerical solutions on finer meshes with $\Delta x=1/200$, $1/400$, $1/800$, and $1/1600$, and plot the obtained results in Figure 4.7 (middle). As one can see, the computed solutions remain stable and well resolved as the mesh

is refined. We also repeat the same finer mesh computations, but using the larger value $\mathtt{C} = 0.25$. We plot the obtained results in Figure 4.7 (right), where one can see that the magnitude of oscillations increases as Δx shrinks, which clearly demonstrates that the coarse-mesh tuning process works in a robust way.

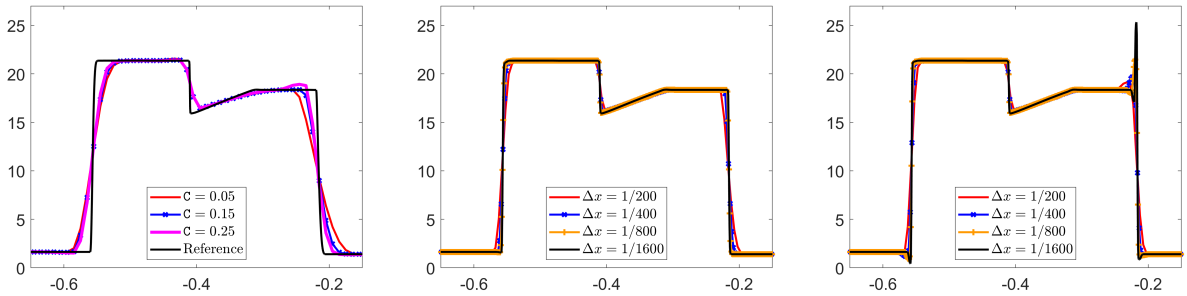

Fig. 4.7. Example 4: Density ρ (zoom at $x \in [-0.65, -0.15]$) computed by the AAAD2 scheme with $\mathtt{C} = 0.05$, 0.15, and 0.25 on the uniform mesh with $\Delta x = 1/100$ (left) and with $\mathtt{C} = 0.15$ (middle) and $\mathtt{C} = 0.25$ (right) on finer uniform meshes with $\Delta x = 1/200$, $1/400$, $1/800$, and $1/1600$.

Example 5—Lax Problem. In this example taken from [31], we consider the Riemann problem with the initial conditions,

$$(\rho, u, p)(x, 0) = \begin{cases} (0.445, 0.31061, 8.928), & x < 0, \\ (0.5, 0, 0.571), & x \geq 0, \end{cases}$$

prescribed in the interval $[-5, 5]$ subject to the free boundary conditions.

We compute the numerical solutions until the final time $t = 1.3$ by the studied AAAD2 (with the adaptation constant $\mathtt{C} = 0.1$) and AAAD5 (with the adaptation constant $\mathtt{C} = 0.5$) schemes on a uniform mesh with $\Delta x = 1/20$. We plot the results in Figures 4.8–4.9 together with the exact solution. As can be seen, both adaptive schemes provide improved resolution of the contact wave compared with their non-adaptive counterparts.

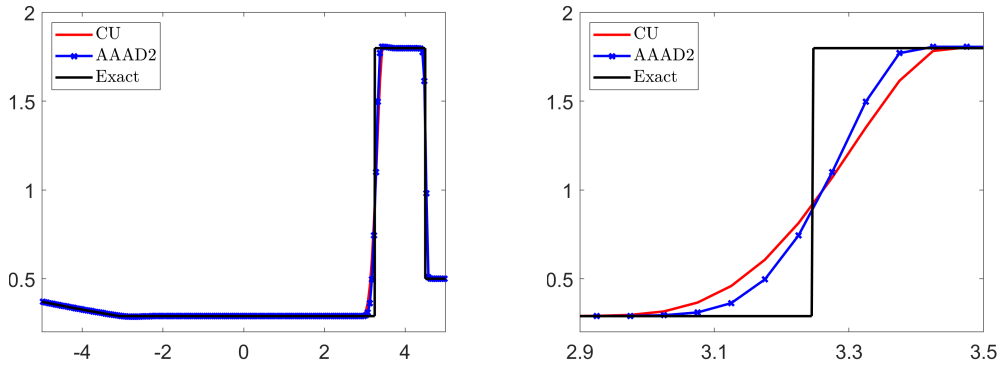

Fig. 4.8. Example 5: Density ρ computed by the CU and AAAD2 schemes (left) and zoom at $x \in [2.9, 3.5]$ (right).

Example 6—Blast Wave Problem. In the last 1-D example, we consider a strong-shock interaction problem from [52], which is considered in the interval $[0, 1]$ with the solid wall boundary conditions and subject to the following initial conditions:

$$(\rho, u, p)\Big|_{(x,0)} = \begin{cases} (1, 0, 1000), & x < 0.1, \\ (1, 0, 0.01), & 0.1 \leq x \leq 0.9, \\ (1, 0, 100), & x > 0.9. \end{cases}$$

We compute the numerical solutions until the final time $t = 0.038$ by the studied AAAD2 scheme (with the adaptation constant $\mathtt{C} = 0.55$) on a uniform mesh with $\Delta x = 1/400$ and AAAD5 scheme (with

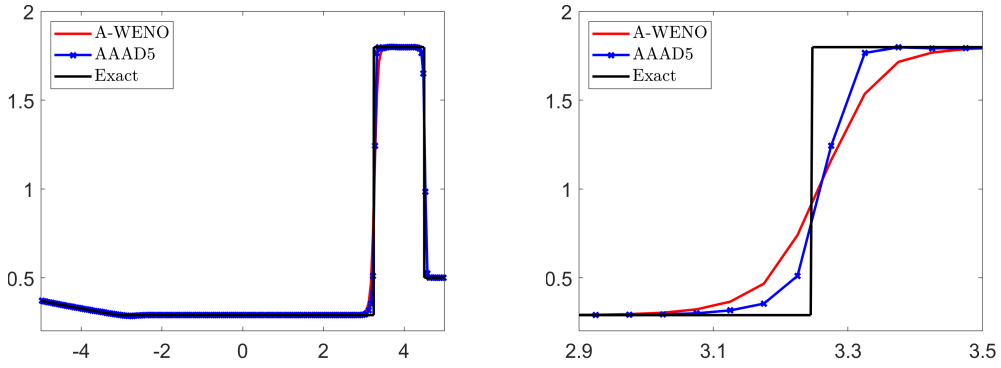

FIG. 4.9. Example 5: Density ρ computed by the A-WENO and AAAD5 schemes (left) and zoom at $x \in [2.9, 3.5]$ (right).

the adaptation constant $\mathtt{C} = 0.5$) on a coarser uniform mesh with $\Delta x = 1/200$. The obtained results are presented in Figures 4.10–4.11 along with a reference solution computed by the CU scheme on a much finer mesh with $\Delta x = 1/4000$. One can see that both AAAD2 and AAAD5 schemes achieve substantial improvement in the quality of the computed solutions.

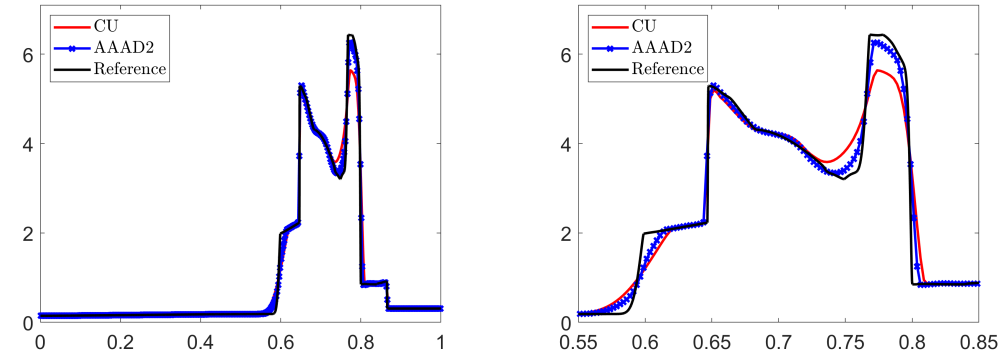

FIG. 4.10. Example 6: Density ρ computed by the CU and AAAD2 schemes with $\Delta x = 1/400$ (left) and zoom at $x \in [0.55, 0.85]$ (right).

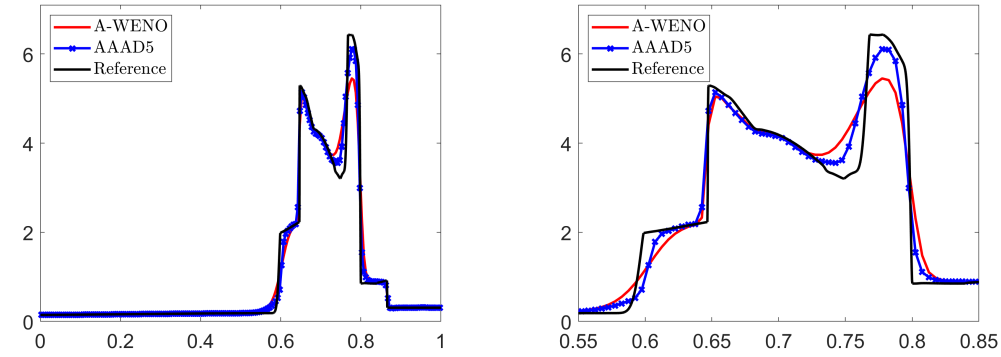

FIG. 4.11. Example 6: Density ρ computed by the A-WENO and AAAD5 schemes with $\Delta x = 1/200$ (left) and zoom at $x \in [0.55, 0.85]$ (right).

4.2. Two-Dimensional Examples. We now turn to the 2-D Euler equations of gas dynamics. In Examples 7–13, we take $\gamma = 1.4$, while in Example 14, we take $\gamma = 5/3$.

Example 7—2-D Accuracy Test. In the first 2-D example taken from [2, 40], we consider the following smooth initial data:

$$\rho(x,y,0)=\left(1-\frac{(\gamma-1)\kappa^2}{2\gamma}\right)^{\frac{1}{\gamma-1}},\quad p(x,y,0)=\rho^\gamma(x,y,0),$$
$$u(x,y,0)=1-\kappa y,\quad v(x,y,0)=1+\kappa x,\quad \kappa=\frac{5}{2\pi}e^{\frac{1-x^2-y^2}{2}}$$

subject to the periodic boundary conditions in the computational domain $[-10,10]\times[-10,10]$. The exact solution of this initial value problem is given by $\boldsymbol{U}(x,y,t)=\boldsymbol{U}(x-t,y-t,0)$.

We compute the numerical solution until the final time $t=0.1$ using the studied AAAD2 and AAAD5 schemes (both with the adaptation constant $\mathtt{C}=0.1$) on a sequence of uniform meshes with $\Delta x=\Delta y=1/10$, $1/20$, and $1/40$, and then measure the L^1-errors and the corresponding experimental convergence rates for the density. The obtained results are presented in Table 4.2, where one can see that the expected orders of accuracy have been achieved by both of the studied schemes.

$\Delta x=\Delta y$	AAAD2		AAAD5	
	Error	Rate	Error	Rate
1/10	3.62e-03	—	3.73e-05	—
1/20	8.18e-04	2.15	1.14e-06	5.04
1/40	1.69e-04	2.27	2.44e-08	5.55

Table 4.2
Example 7: The L^1-errors of the density ρ and experimental convergence rates for the AAAD2 and AAAD5 schemes.

Remark 4.2. As in Example 1, we use smaller time steps with $\Delta t\sim\min\{(\Delta x)^{5/3},(\Delta y)^{5/3}\}$ in order to achieve fifth order of accuracy by the AAAD5 scheme.

Example 8—Explosion Problem. In this example taken from [32], we consider the explosion problem. The initial conditions,

$$(\rho(x,y,0),u(x,y,0),v(x,y,0),p(x,y,0))=\begin{cases}(1,0,0,1), & x^2+y^2<0.16,\\ (0.125,0,0,0.1), & \text{otherwise},\end{cases}$$

are prescribed in $[-1.5,1.5]\times[-1.5,1.5]$ subject to the free boundary conditions. The solution develops circular shock and contact waves, with the latter one being unstable.

We compute the numerical solutions until the final time $t=3.2$ by the studied AAAD2 (with the adaptation constant $\mathtt{C}=0.03$) and AAAD5 (with the adaptation constant $\mathtt{C}=0.02$) schemes on a uniform mesh with $\Delta x=\Delta y=3/800$. The obtained results are presented in Figure 4.12, where one can clearly observe noticeable differences between the CU and A-WENO schemes and their AAAD counterparts: the adaptive solutions exhibit substantially more small-scale structures and a wider mixing layer, while the main shock remains stable.

Example 9—2-D Riemann Problem (Configuration 3). In this example, we consider Configuration 3 of the 2-D Riemann problems from [29] with the initial conditions

$$(\rho,u,v,p)(x,y,0)=\begin{cases}(1.5,0,0,1.5), & x>1,\ y>1,\\ (0.5323,1.206,0,0.3), & x<1,\ y>1,\\ (0.138,1.206,1.206,0.029), & x<1,\ y<1,\\ (0.5323,0,1.206,0.3), & x>1,\ y<1,\end{cases}$$

prescribed in $[0,1.2]\times[0,1.2]$ subject to the free boundary conditions.

We compute the numerical solution until the final time $t=1$ by the studied AAAD2 (with the adaptation constant $\mathtt{C}=0.04$) and AAAD5 (with the adaptation constant $\mathtt{C}=0.02$) schemes on a

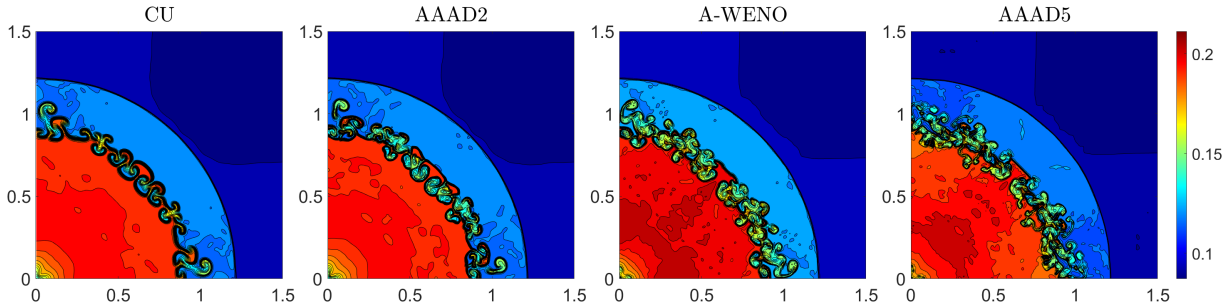

FIG. 4.12. Example 8: Density ρ computed by the CU, AAAD2, A-WENO, and AAAD5 schemes.

uniform mesh with $\Delta x = \Delta y = 1/500$ and plot the results in Figure 4.13. As one can see, the AAAD schemes outperform their non-adaptive counterparts in capturing the sideband instability of the jet, in particular, in the zones of strong along-jet velocity shear and near the jet neck.

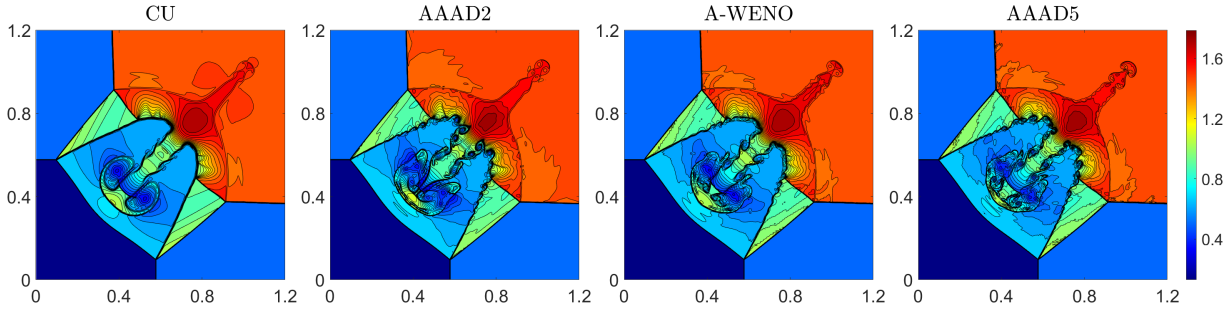

FIG. 4.13. Example 9: Density ρ computed by the CU, AAAD2, A-WENO, and AAAD5 schemes.

We use this example to illustrate the tuning procedure for $\mathtt{C}$ in the 2-D setting. To this end, we proceed as in the 1-D case: we first tune $\mathtt{C}$ on a coarse mesh and then use the selected values for fine-mesh computations. We begin by computing the coarse-mesh numerical solutions with $\Delta x = \Delta y = 3/1000$ using $\mathtt{C} = 0.02$, 0.04, 0.06, and 0.08, and plot the results in Figure 4.14, where one can see that $\mathtt{C} = 0.04$ seems to be a reasonable choice as the use of larger values of $\mathtt{C}$ leads to the appearance of certain unstable structures. We then verify that the value $\mathtt{C} = 0.04$ can be safely used on finer meshes with $\Delta x = \Delta y = 3/2000$, $3/2500$, $1/1000$, and $3/3500$; see Figure 4.15. We have also run the AAAD2 scheme with $\mathtt{C} = 0.06$ on finer meshes, but when the mesh is refined, the magnitude of oscillations grows and negative pressure values start appearing.

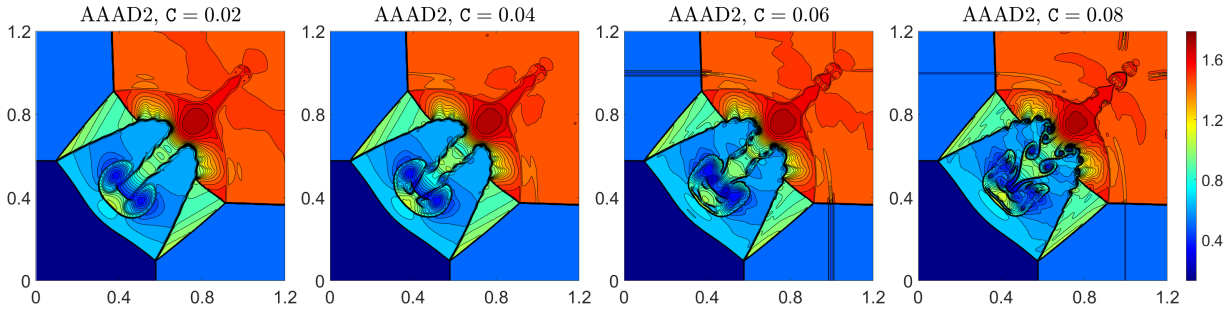

FIG. 4.14. Example 9: Density ρ computed by the AAAD2 scheme with $\Delta x = \Delta y = 3/1000$ for $\mathtt{C} = 0.02$, 0.04, 0.06, and 0.08.

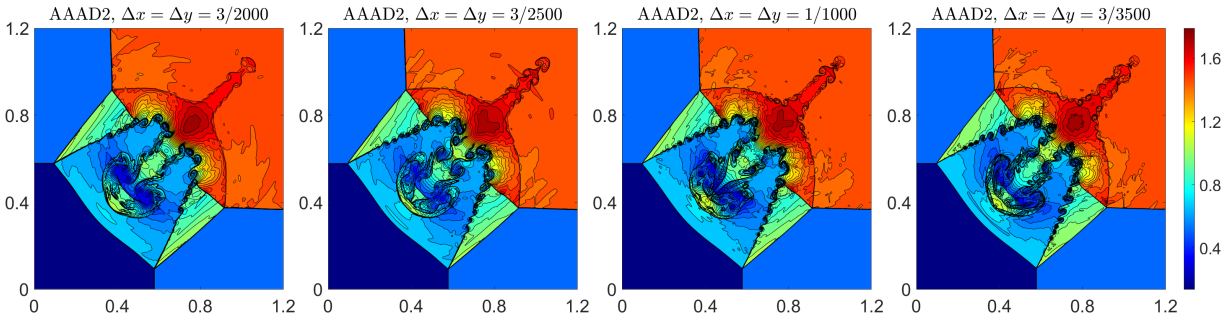

Fig. 4.15. Example 9: Density ρ computed by the AAAD2 scheme on uniform meshes with $\Delta x = \Delta y = 3/2000$, $3/2500$, $1/1000$, and $3/3500$ with $\texttt{C} = 0.04$.

Example 10—2-D Riemann Problem (Configuration 6). In this example, we consider Configuration 6 of the 2-D Riemann problems taken from [29] with the initial conditions

$$(\rho,u,v,p)(x,y,0) = \begin{cases} (1,0.75,-0.5,1), & x>0.5,\ y>0.5,\\ (2,0.75,0.5,1), & x<0.5,\ y>0.5,\\ (1,-0.75,0.5,1), & x<0.5,\ y<0.5,\\ (3,-0.75,-0.5,1), & x>0.5,\ y<0.5, \end{cases}$$

prescribed in $[0,1]\times[0,1]$ subject to the free boundary conditions.

We compute the numerical solution until the final time $t = 1$ by the studied AAAD2 (with the adaptation constant $\texttt{C} = 0.05$) and AAAD5 (with the adaptation constant $\texttt{C} = 0.02$) schemes on a uniform mesh with $\Delta x = \Delta y = 1/400$ and plot the results in Figure 4.16. As one can see, the AAAD schemes capture more intricate vortex structures than their non-adaptive counterparts, which indicates higher resolution and reduced numerical dissipation of the proposed AAAD schemes. One can also observe that the second-order AAAD2 scheme achieves higher resolution than the fifth-order A-WENO scheme. This demonstrates a powerful feature of the proposed AAAD strategy.

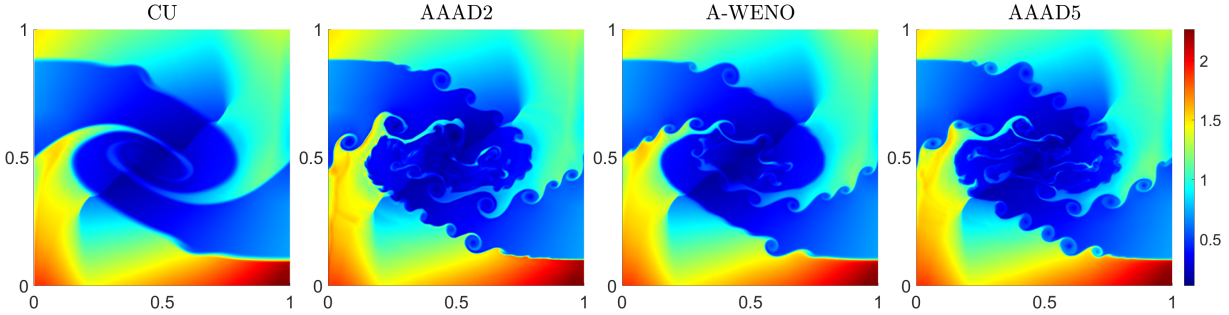

Fig. 4.16. Example 10: Density ρ computed by the CU, AAAD2, A-WENO, and AAAD5 schemes.

Example 11—2-D Riemann Problem (Configuration 12). In this example, we consider Configuration 12 of the 2-D Riemann problems taken from [29] with the initial conditions

$$(\rho,u,v,p)\big|_{(x,y,0)} = \begin{cases} (0.5313,0,0,0.4), & x>0.5,\ y>0.5,\\ (1,0.7276,0,1), & x<0.5,\ y>0.5,\\ (0.8,0,0,1), & x<0.5,\ y<0.5,\\ (1,0,0.7276,1), & x>0.5,\ y<0.5, \end{cases}$$

prescribed in the computational domain $[0,0.6]\times[0,0.6]$ subject to the free boundary conditions.

We compute the numerical solution until the final time $t = 1$ by the studied AAAD2 (with the adaptation constant $\texttt{C} = 0.04$) and AAAD5 (with the adaptation constant $\texttt{C} = 0.02$) schemes on a

uniform mesh with $\Delta x = \Delta y = 1/1000$ and plot the obtained results in Figure 4.17. One can see that the AAAD schemes resolve more vortices arising along the unstable contact surfaces than their non-adaptive counterparts. As in the previous example, we notice that the second-order AAAD2 scheme clearly outperforms the fifth-order A-WENO scheme.

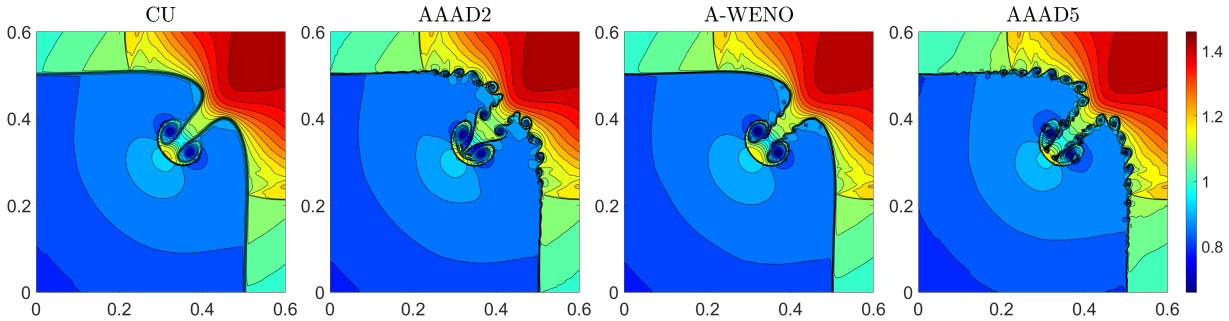

FIG. 4.17. Example 11: Density ρ computed by the CU, AAAD2, A-WENO, and AAAD5 schemes.

Example 12—Implosion Problem. In this example, we consider the implosion problem taken from [32]; see also [4, 25]. The initial conditions

$$(\rho(x,y,0), u(x,y,0), v(x,y,0), p(x,y,0)) = \begin{cases} (0.125, 0, 0, 0.14), & |x| + |y| < 0.15, \\ (1, 0, 0, 1), & \text{otherwise}, \end{cases}$$

are prescribed in $[0, 0.3] \times [0, 0.3]$ subject to the solid boundary conditions. In this problem, a jet forms near the origin and propagates along the diagonal $y = x$. Excessive numerical diffusion may smear the jet or alter its propagation speed, and therefore this example is often used to assess numerical dissipation present in studied schemes.

We compute the numerical solution until the final time $t = 2.5$ by the studied AAAD2 (with the adaptation constant $\texttt{C} = 0.05$) and AAAD5 (with the adaptation constant $\texttt{C} = 0.01$) schemes on a uniform mesh with $\Delta x = \Delta y = 1/1500$. The obtained results are plotted in Figure 4.18, where one can observe that the jets propagate substantially farther along the diagonal by the AAAD schemes: This indicates that they are less diffusive than their non-adaptive counterparts. As in several previous examples, we notice that the second-order AAAD2 scheme clearly outperforms the fifth-order A-WENO scheme.

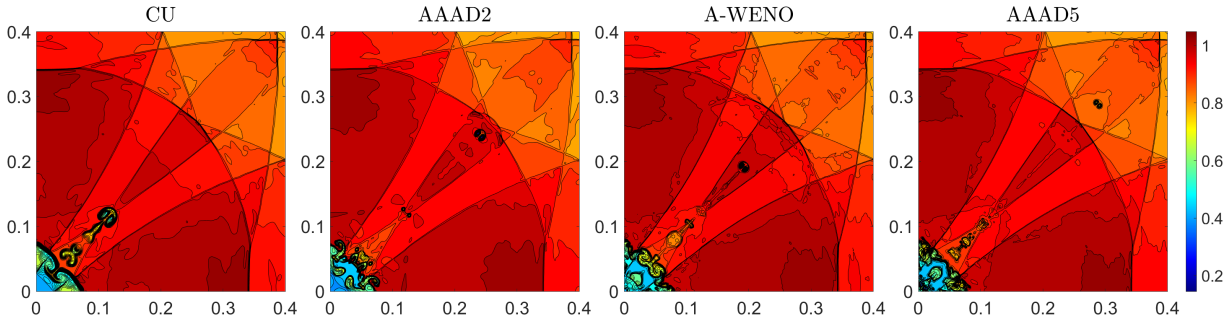

FIG. 4.18. Example 12: Density ρ computed by the CU, AAAD2, A-WENO, and AAAD5 schemes.

Example 13—Kelvin-Helmholtz (KH) Instability. In this example, we study the KH instability problem taken from [36]. We consider the initial data

$$(\rho(x,y,0),u(x,y,0)) = \begin{cases} (1,-0.5+0.5e^{(y+0.25)/L}), & y<-0.25,\\ (2,0.5-0.5e^{(-y-0.25)/L}), & -0.25<y<0,\\ (2,0.5-0.5e^{(y-0.25)/L}), & 0<y<0.25,\\ (1,-0.5+0.5e^{(0.25-y)/L}), & y>0.25, \end{cases} \tag{4.1}$$
$$v(x,y,0)=0.01\sin(4\pi x),\quad p(x,y,0)\equiv 1.5,$$

in $[-0.5,0.5]\times[-0.5,0.5]$ subject to the periodic boundary conditions. In (4.1), $L=0.00625$ is a smoothing parameter.

We compute the numerical solution until the final time $t=4$ by the studied AAAD2 (with the adaptation constant `C` $=0.05$) and AAAD5 (with the adaptation constant `C` $=0.01$) schemes on a uniform mesh with $\Delta x=\Delta y=1/1024$ and plot the numerical results at times $t=1$, 2.5, and 4 in Figures 4.19–4.20. One can observe that already at $t=1$, the vortex streets produced by the AAAD schemes are more pronounced. These structures grow over time, leading to increasingly complex mixing patterns at later times. Overall, the AAAD schemes outperform their non-adaptive counterparts by capturing richer turbulent structures.

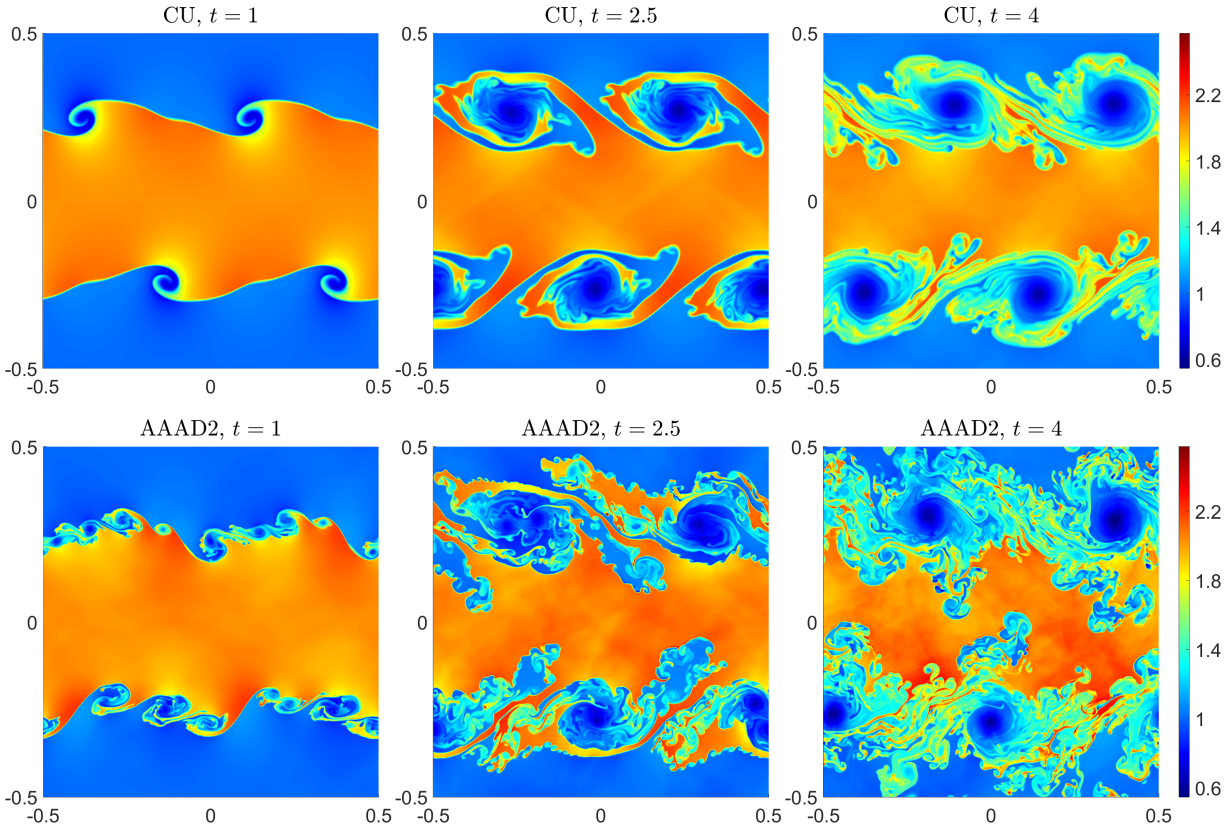

Fig. 4.19. Example 13: Density ρ computed by the CU (top row) and AAAD2 (bottom row) schemes at $t=1$ (left column), 2.5 (middle column), and 4 (right column).

Example 14—Rayleigh-Taylor (RT) Instability. In the last example taken from [39], we investigate the RT instability, which occurs when a layer of heavier fluid is placed above a layer of lighter fluid. The model is governed by the 2-D Euler equations with gravitational source terms acting in the positive

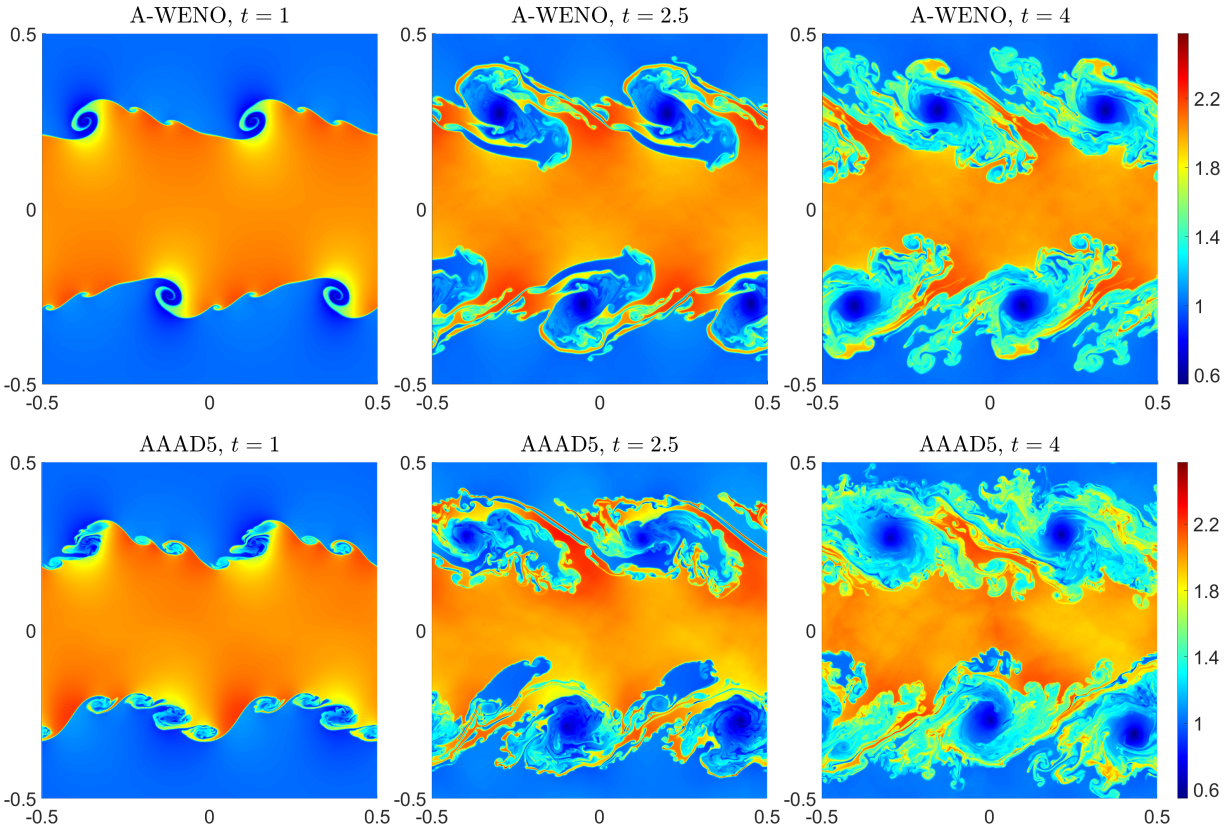

FIG. 4.20. Example 13: Density ρ computed by the A-WENO (top row) and AAAD5 (bottom row) schemes at $t = 1$ (left column), 2.5 (middle column), and 4 (right column).

y-direction, namely,

$$\begin{aligned}
&\rho_t + (\rho u)_x + (\rho v)_y = 0,\\
&(\rho u)_t + (\rho u^2 + p)_x + (\rho uv)_y = 0,\\
&(\rho v)_t + (\rho uv)_x + (\rho v^2 + p)_y = \rho,\\
&E_t + [u(E+p)]_x + [v(E+p)]_y = \rho v.
\end{aligned}$$

We consider the initial conditions

$$(\rho(x,y,0), u(x,y,0), v(x,y,0), p(x,y,0)) = \begin{cases} (2, 0, -0.025\,c\cos(8\pi x), 2y+1), & y < 0.5,\\ (1, 0, -0.025\,c\cos(8\pi x), y+1.5), & \text{otherwise,}\end{cases}$$

where c is the speed of sound. The computational domain is $[0, 0.25] \times [0, 1]$ with the solid wall boundary conditions imposed at $x = 0$ and $x = 0.25$, and the following Dirichlet boundary conditions imposed at the top and bottom boundaries:

$$(\rho, u, v, p)\big|_{y=1} = (1, 0, 0, 2.5), \quad (\rho, u, v, p)\big|_{y=0} = (2, 0, 0, 1).$$

We compute the numerical solution until the final time $t = 2.95$ by the studied AAAD2 (with the adaptation constant $\mathtt{C} = 0.05$) and AAAD5 (with the adaptation constant $\mathtt{C} = 0.02$) schemes on a uniform mesh with $\Delta x = \Delta y = 1/1024$ and plot the results, obtained at times $t = 1.95$ and 2.95, in Figure 4.21. One can observe pronounced differences between the AAAD solutions and those computed by the CU and A-WENO schemes: the AAAD schemes capture substantially more complex small-scale structures, which again indicates reduced numerical dissipation present in the AAAD schemes.

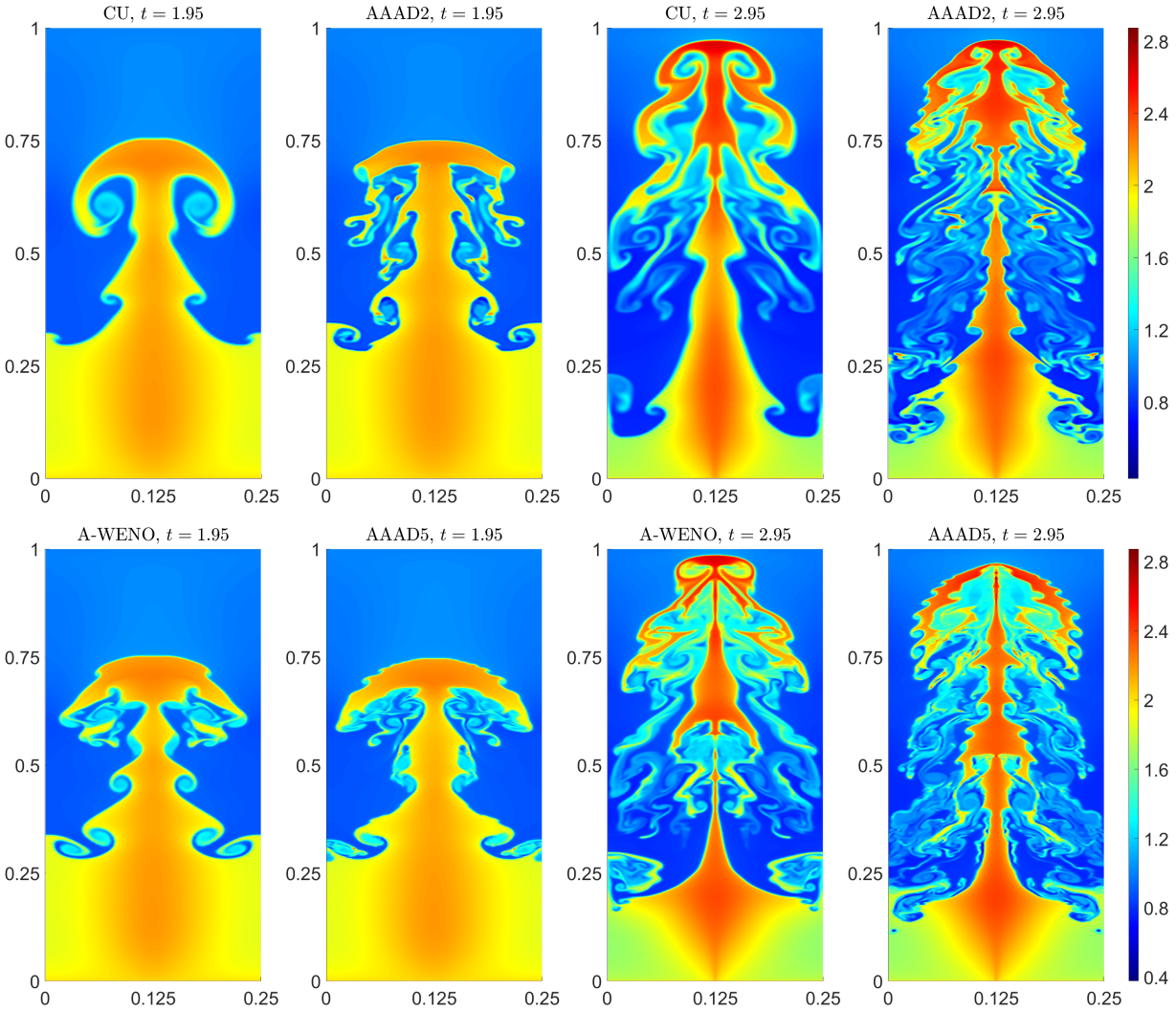

FIG. 4.21. Example 14: Density ρ computed by the CU, AAAD2, A-WENO, and AAAD5 schemes at different times.

Appendix A. 1-D Local Characteristic Decomposition Based Fifth-Order WENO-Z Interpolant. In this appendix, we briefly describe the 1-D LCD based fifth-order WENO-Z interpolant.

Given the point values ψ_j of a certain function ψ at uniform grid points $x = x_j$, the values $\psi^-_{j+\frac{1}{2}}$ are computed using a weighted average of the three parabolic interpolants $\mathcal{P}_0(x)$, $\mathcal{P}_1(x)$ and $\mathcal{P}_2(x)$ obtained using the stencils $[x_{j-2}, x_{j-1}, x_j]$, $[x_{j-1}, x_j, x_{j+1}]$, and $[x_j, x_{j+1}, x_{j+2}]$, respectively:

$$\psi^-_{j+\frac{1}{2}} = \sum_{k=0}^{2} \omega_k \mathcal{P}_k(x_{j+\frac{1}{2}}), \tag{A.1}$$

where

$$\begin{aligned}
\mathcal{P}_0(x_{j+\frac{1}{2}}) &= \frac{3}{8}\psi_{j-2} - \frac{5}{4}\psi_{j-1} + \frac{15}{8}\psi_j,\\
\mathcal{P}_1(x_{j+\frac{1}{2}}) &= -\frac{1}{8}\psi_{j-1} + \frac{3}{4}\psi_j + \frac{3}{8}\psi_{j+1},\\
\mathcal{P}_2(x_{j+\frac{1}{2}}) &= \frac{3}{8}\psi_j + \frac{3}{4}\psi_{j+1} - \frac{1}{8}\psi_{j+2}.
\end{aligned} \tag{A.2}$$

To ensure (A.1)–(A.2) are fifth-order accurate and nonoscillatory, we take the following weights ω_k in

(A.1):

$$\omega_k := \frac{\alpha_k}{\alpha_0+\alpha_1+\alpha_2}, \quad \alpha_k = d_k\left[1+\left(\frac{\tau_5}{\beta_k+\varepsilon}\right)^p\right], \quad \tau_5 = |\beta_2-\beta_0|, \tag{A.3}$$

where $d_0=\frac{1}{16}$, $d_1=\frac{5}{8}$, and $d_2=\frac{5}{16}$, and the SIs β_k are given by

$$\begin{aligned}
\beta_0 &= \frac{13}{12}\big(\psi_{j-2}-2\psi_{j-1}+\psi_j\big)^2+\frac{1}{4}\big(\psi_{j-2}-4\psi_{j-1}+3\psi_j\big)^2,\\
\beta_1 &= \frac{13}{12}\big(\psi_{j-1}-2\psi_j+\psi_{j+1}\big)^2+\frac{1}{4}\big(\psi_{j-1}-\psi_{j+1}\big)^2,\\
\beta_2 &= \frac{13}{12}\big(\psi_j-2\psi_{j+1}+\psi_{j+2}\big)^2+\frac{1}{4}\big(3\psi_j-4\psi_{j+1}+\psi_{j+2}\big)^2.
\end{aligned} \tag{A.4}$$

In this paper, we have used $p=2$ and $\varepsilon=10^{-12}$ in all of the numerical examples. The corresponding right-sided value, $\psi^+_{j+\frac{1}{2}}$, can also be derived using a mirror-symmetric approach, and we omit it for the sake of brevity.

To ensure a nonoscillatory nature of the reconstruction (A.1)–(A.4), we apply it to the local characteristic variables, which we introduce in the neighborhood of $x=x_{j+\frac{1}{2}}$:

$$\boldsymbol{\Gamma}_\ell = \big(R_{j+\frac{1}{2}}\big)^{-1}\boldsymbol{U}_{j+\ell}, \quad \ell=-2,\ldots,3.$$

Equipped with the values $\boldsymbol{\Gamma}_{-2}$, $\boldsymbol{\Gamma}_{-1}$, $\boldsymbol{\Gamma}_0$, $\boldsymbol{\Gamma}_1$, $\boldsymbol{\Gamma}_2$, and $\boldsymbol{\Gamma}_3$, we then apply the interpolation procedure (A.1)–(A.4) to each of the components $\Gamma^{(i)}$, $i=1,\ldots,d$ of $\boldsymbol{\Gamma}$ to obtain $\boldsymbol{\Gamma}^-_{\frac{1}{2}}$ (the values of $\boldsymbol{\Gamma}^+_{\frac{1}{2}}$ are computed in the mirror-symmetric way). Finally, the corresponding one-sided point values of $\boldsymbol{U}$ are given by

$$\boldsymbol{U}^\pm_{j+\frac{1}{2}} = R_{j+\frac{1}{2}}\boldsymbol{\Gamma}^\pm_{\frac{1}{2}}.$$

REFERENCES

[1] F. Aràndiga, A. Baeza, and R. Donat, *Vector cell-average multiresolution based on Hermite interpolation*, Adv. Comput. Math., 28 (2008), pp. 1–22.

[2] W. Boscheri and M. Dumbser, *Arbitrary-Lagrangian-Eulerian one-step WENO finite volume schemes on unstructured triangular meshes*, Commun. Comput. Phys., 14 (2013), pp. 1174–1206.

[3] E. J. Caramana, M. J. Shashkov, and P. P. Whalen, *Formulations of artificial viscosity for multi-dimensional shock wave computations*, J. Comput. Phys., 144 (1998), pp. 70–97.

[4] A. Chertock, S. Chu, M. Herty, A. Kurganov, and M. Lukáčová-Medviďová, *Local characteristic decomposition based central-upwind scheme*, J. Comput. Phys., 473 (2023). Paper No. 111718.

[5] A. Chertock, S. Chu, and A. Kurganov, *Adaptive high-order A-WENO schemes based on a new local smoothness indicator*, East Asian J. Appl. Math., 13 (2023), pp. 576–609.

[6] A. Chertock, S. Cui, A. Kurganov, S. N. Özcan, and E. Tadmor, *Well-balanced schemes for the Euler equations with gravitation: conservative formulation using global fluxes*, J. Comput. Phys., 358 (2018), pp. 36–52.

[7] S. Chu, M. Herty, and A. Kurganov, *A new smoothness indicator*. In preparation.

[8] S. Chu, A. Kurganov, and R. Xin, *A fifth-order A-WENO scheme based on the low-dissipation central-upwind fluxes*, in Hyperbolic Problems: Theory, Numerics, Applications. Vol. II, vol. 35 of SEMA SIMAI Springer Ser., Springer, Cham, 2024, pp. 51–61.

[9] J. Dewar, A. Kurganov, and M. Leopold, *Pressure-based adaption indicator for compressible Euler equations*, Numer. Methods Partial Differential Equations, 31 (2015), pp. 1844–1874.

[10] M. Dumbser, O. Zanotti, R. Loubère, and S. Diot, *A posteriori subcell limiting of the discontinuous Galerkin finite element method for hyperbolic conservation laws*, J. Comput. Phys., 278 (2014), pp. 47–75.

[11] G. Fu and C.-W. Shu, *A new troubled-cell indicator for discontinuous Galerkin methods for hyperbolic conservation laws*, J. Comput. Phys., 347 (2017), pp. 305–327.

[12] Z. Gao, Q. Liu, J. S. Hesthaven, B.-S. Wang, W. S. Don, and X. Wen, *Non-intrusive reduced order modeling of convection dominated flows using artificial neural networks with application to Rayleigh-Taylor instability*, Commun. Comput. Phys., 30 (2021), pp. 97–123.

[13] A. Gelb and E. Tadmor, *Spectral reconstruction of piecewise smooth functions from their discrete data*, M2AN Math. Model. Numer. Anal., 36 (2002), pp. 155–175.

[14] A. Gelb and E. Tadmor, *Adaptive edge detectors for piecewise smooth data based on the minmod limiter*, J. Sci. Comput., 28 (2006), pp. 279–306.

[15] S. Gottlieb, D. Ketcheson, and C.-W. Shu, *Strong stability preserving Runge-Kutta and multistep time discretizations*, World Scientific Publishing Co. Pte. Ltd., Hackensack, NJ, 2011.

[16] S. Gottlieb, C.-W. Shu, and E. Tadmor, *Strong stability-preserving high-order time discretization methods*, SIAM Rev., 43 (2001), pp. 89–112.
[17] J.-L. Guermond and R. Pasquetti, *Entropy-based nonlinear viscosity for Fourier approximations of conservation laws*, C. R. Math. Acad. Sci. Paris, 346 (2008), pp. 801–806.
[18] J.-L. Guermond, R. Pasquetti, and B. Popov, *Entropy viscosity method for nonlinear conservation laws*, J. Comput. Phys., 230 (2011), pp. 4248–4267.
[19] A. Harten, *ENO schemes with subcell resolution*, J. Comput. Phys., 83 (1989), pp. 148–184.
[20] R. Hartmann and P. Houston, *Adaptive discontinuous Galerkin finite element methods for nonlinear hyperbolic conservation laws*, SIAM J. Sci. Comput., 24 (2002), pp. 979–1004.
[21] R. Hartmann and P. Houston, *Adaptive discontinuous Galerkin finite element methods for the compressible Euler equations*, J. Comput. Phys., 183 (2002), pp. 508–532.
[22] Y. Jiang, C.-W. Shu, and M. Zhang, *An alternative formulation of finite difference weighted ENO schemes with Lax-Wendroff time discretization for conservation laws*, SIAM J. Sci. Comput., 35 (2013), pp. A1137–A1160.
[23] S. Karni, A. Kurganov, and G. Petrova, *A smoothness indicator for adaptive algorithms for hyperbolic systems*, J. Comput. Phys., 178 (2002), pp. 323–341.
[24] V. A. Kolotilov, A. A. Kurganov, V. V. Ostapenko, N. A. Khandeeva, and S. Chu, *On the accuracy of shock-capturing schemes calculating gas-dynamic shock waves*, Comput. Math. Math. Phys., 63 (2023), pp. 1341–1349.
[25] A. Kurganov and C.-T. Lin, *On the reduction of numerical dissipation in central-upwind schemes*, Commun. Comput. Phys., 2 (2007), pp. 141–163.
[26] A. Kurganov and Y. Liu, *New adaptive artificial viscosity method for hyperbolic systems of conservation laws*, J. Comput. Phys., 231 (2012), pp. 8114–8132.
[27] A. Kurganov, P. Noelle, and G. Petrova, *Semidiscrete central-upwind schemes for hyperbolic conservation laws and Hamilton-Jacobi equations*, SIAM J. Sci. Comput., 23 (2001), pp. 707–740.
[28] A. Kurganov and E. Tadmor, *New high-resolution semi-discrete central schemes for Hamilton-Jacobi equations*, J. Comput. Phys., 160 (2000), pp. 720–742.
[29] A. Kurganov and E. Tadmor, *Solution of two-dimensional Riemann problems for gas dynamics without Riemann problem solvers*, Numer. Methods Partial Differential Equations, 18 (2002), pp. 584–608.
[30] A. Kurganov and R. Xin, *New low-dissipation central-upwind schemes*, J. Sci. Comput., 96 (2023). Paper No. 56.
[31] P. D. Lax, *Hyperbolic Systems of Conservation Laws and the Mathematical Theory of Shock Waves*, SIAM, Philadelphia, 1973.
[32] R. Liska and B. Wendroff, *Comparison of several difference schemes on 1D and 2D test problems for the Euler equations*, SIAM J. Sci. Comput., 25 (2003), pp. 995–1017.
[33] H. Liu, *A numerical study of the performance of alternative weighted ENO methods based on various numerical fluxes for conservation law*, Appl. Math. Comput., 296 (2017), pp. 182–197.
[34] H. Liu and J. Qiu, *Finite difference Hermite WENO schemes for conservation laws, II: An alternative approach*, J. Sci. Comput., 66 (2016), pp. 598–624.
[35] R. Löhner, *An adaptive finite element scheme for transient problems in CFD*, Comput. Methods Appl. Mech. Eng., 61 (1987), pp. 323–338.
[36] J. Panuelos, J. Wadsley, and N. Kevlahan, *Low shear diffusion central schemes for particle methods*, J. Comput. Phys., 414 (2020). Paper No. 109454.
[37] G. Puppo and M. Semplice, *Numerical entropy and adaptivity for finite volume schemes*, Commun. Comput. Phys., 10 (2011), pp. 1132–1160.
[38] J. Qiu and C.-W. Shu, *A comparison of troubled-cell indicators for Runge-Kutta discontinuous Galerkin methods using weighted essentially nonoscillatory limiters*, SIAM J. Sci. Comput., 27 (2005), pp. 995–1013.
[39] J. Shi, Y.-T. Zhang, and C.-W. Shu, *Resolution of high order WENO schemes for complicated flow structures*, J. Comput. Phys., 186 (2003), pp. 690–696.
[40] C.-W. Shu, *Essentially non-oscillatory and weighted essentially non-oscillatory schemes for hyperbolic conservation laws*, in Advanced numerical approximation of nonlinear hyperbolic equations (Cetraro, 1997), vol. 1697 of Lecture Notes in Math., Springer, Berlin, 1998, pp. 325–432.
[41] C.-W. Shu and S. Osher, *Efficient implementation of essentially non-oscillatory shock-capturing schemes*, J. Comput. Phys., 77 (1988), pp. 439–471.
[42] C.-W. Shu and S. Osher, *Efficient implementation of essentially nonoscillatory shock-capturing schemes. II*, J. Comput. Phys., 83 (1989), pp. 32–78.
[43] A. Szepessy, *Convergence of a shock-capturing streamline diffusion finite element method for a scalar conservation law in two space dimensions*, Math. Comp., 53 (1989), pp. 527–545.
[44] V. A. Titarev and E. F. Toro, *WENO schemes based on upwind and centred TVD fluxes*, Comput. & Fluids, 34 (2005), pp. 705–720.
[45] E. F. Toro and V. A. Titarev, *TVD fluxes for the high-order ADER schemes*, J. Sci. Comput., 24 (2005), pp. 285–309.
[46] J. von Neumann and R. D. Richtmyer, *A method for the numerical calculation of hydrodynamic shocks*, J. Appl. Phys., 21 (1950), pp. 232–237.
[47] M. J. Vuik and J. K. Ryan, *Automated parameters for troubled-cell indicators using outlier detection*, SIAM J. Sci. Comput., 38 (2016), pp. A84–A104.
[48] B.-S. Wang, P. Li, Z. Gao, and W. S. Don, *An improved fifth order alternative WENO-Z finite difference scheme for hyperbolic conservation laws*, J. Comput. Phys., 374 (2018), pp. 469–477.
[49] W. Wang, C.-W. Shu, H. C. Yee, D. V. Kotov, and B. Sjögreen, *High order finite difference methods with subcell resolution for stiff multispecies discontinuity capturing*, Commun. Comput. Phys., 17 (2015), pp. 317–336.
[50] X. Wen, W. S. Don, Z. Gao, and J. S. Hesthaven, *An edge detector based on artificial neural network with*

application to hybrid compact-WENO finite difference scheme, J. Sci. Comput., 83 (2020). Paper No. 49.
[51] M. L. WILKINS, *Use of artificial viscosity in multidimensional fluid dynamic calculations*, J. Comput. Phys., 36 (1980), pp. 281–303.
[52] P. WOODWARD AND P. COLELLA, *The numerical simulation of two-dimensional fluid flow with strong shocks*, J. Comput. Phys., 54 (1984), pp. 115–173.